Coupled myovascular expansion directs cardiac growth and regeneration

Authors: Paige DeBenedittis[1], Anish Karpurapu[1], Albert Henry[2,3], Michael C. Thomas[1], Timothy J. McCord[1], Kyla Brezitski[1], Anil Prasad[1], Yoshihiko Kobayashi[4], Svati H. Shah[1], Christopher D. Kontos[1,5], Purushothama Rao Tata[4,6,7], R. Thomas Lumbers[3,8,9], and Ravi Karra[1,6,7,10,*]

Affiliations:

[1]Division of Cardiology, Department of Medicine, Duke University Medical Center; Durham, NC, USA

[2]Institute of Cardiovascular Science, University College London; London, UK

[3]Institute of Health Informatics, University College London; London, UK

[4]Department of Cell Biology, Duke University; Durham, NC, USA

[5]Department of Pharmacology & Cancer Biology, Duke University; Durham, NC, USA

[6]Regeneration Next, Duke University; Durham, NC, USA

[7]Center for Aging, Duke University Medical Center; Durham, NC, USA

[8]Health Data Research UK London, University College London; London, UK

[9]British Heart Foundation Research Accelerator, University College London; London, UK

[10]Department of Pathology, Duke University Medical Center; Durham, NC, USA

Address correspondence to: Ravi Karra MD MHS
Box 102152 DUMC
Durham, NC 27710
ravi.karra@duke.edu

ABSTRACT

Background: Heart regeneration requires multiple cell types to enable cardiomyocyte (CM) proliferation. How these cells interact to create growth niches is unclear. Here we profile proliferation kinetics of cardiac endothelial cells (CECs) and CMs in the neonatal mouse heart and find that they are spatiotemporally coupled.

Methods and Results: We show that coupled myovascular expansion during cardiac growth or regeneration is dependent upon VEGF-VEGFR2 signaling, as genetic deletion of *Vegfr2* from CECs or inhibition of VEGFA abrogates both CEC and CM proliferation. Repair of cryoinjury displays poor spatial coupling of CEC and CM proliferation. Boosting CEC density after cryoinjury with virus encoding *Vegfa* enhances regeneration. Using Mendelian randomization, we demonstrate that circulating VEGFA levels are positively linked with human myocardial mass, suggesting that *Vegfa* can stimulate human cardiac growth.

Conclusions: Our work demonstrates the importance of coupled CEC and CM expansion and reveals a myovascular niche that may be therapeutically targeted for heart regeneration.

Keywords: Myovascular, heart regeneration, cardiomyocyte proliferation.

Non-standard abbreviations and acronyms: cardiac endothelial cells (CECs), cryoinjury (CI), cardiomyocytes (CMs), genome-wide association study (GWAS), left ventricular (LV), Mendelian randomization (MR), protein quantitative trait loci, (pQTL), single cell RNA-sequencing (scRNA-Seq)

INTRODUCTION

In many organs, heterologous cell types establish specialized microenvironments, or niches, that mediate tissue growth and regeneration. Alterations to niche constituents can affect the efficiency of tissue growth and outcomes after injury, making niches a possible target for therapeutic regeneration (1, 2). For organs like the intestines, bone marrow, skin, and skeletal muscle, niches are classically centered around a stem cell compartment (3). With a few notable exceptions, niches within organs that lack a resident stem cell are less defined. For instance, in the developing and regenerating neonatal mouse heart, hypoxic niches have been associated with regionalized growth, but the cellular makeup of these niches is unclear (4).

Studies in zebrafish, salamanders, and neonatal mice have established a template for innate heart regeneration through proliferation of spared cardiomyocytes (CMs) (5-8). However, innate heart regeneration is a multicellular process with required contributions from epicardial cells, inflammatory cells, and nerves (9-11). Recent work has highlighted a critical role for the vasculature in heart regeneration (12-15). In zebrafish and neonatal mice, cardiac endothelial cells (CECs) rapidly respond to injury, extending nascent vessels into the wound that ultimately guide CM growth (14, 16, 17). Lineage tracing studies have demonstrated that these new vessels form by proliferation of CECs (16-18). Functional interference with angiogenic responses in the zebrafish or the neonatal mouse heart is associated with defects in CM proliferation (14, 17). Conversely, overexpression of the master angiogenic factor, *vegfaa*, is sufficient to induce ectopic cardiac growth in zebrafish, suggesting that a stimulated vasculature instructs cardiac growth (19). However, a similar role for VEGFA-stimulated CECs in the mammalian heart has yet to be shown.

Here, we spatiotemporally model CM and CEC proliferation in the neonatal mouse heart to investigate the mechanisms underlying cardiac growth and regeneration. We find that CM and CEC proliferation are tightly coupled during postnatal cardiac growth. With cryoinjury (CI), a model of incomplete regeneration, this coupling is spatially impaired. We demonstrate that coupled myovascular expansion is dependent on VEGFA signaling to endothelial VEGFR2 and restoration of coupling after CI through exogenous *Vegfa* can enhance regeneration. Similarly, we find that genetically-determined levels of circulating VEGFA are associated with higher myocardial mass in humans, suggesting that VEGFA also regulates human myocardial growth. Together, these data demonstrate that coupled expansion of CECs and CMs within a myovascular niche regulates cardiac growth and regeneration.

RESULTS

Spatiotemporal coupling of EdU$^+$ CECs and EdU$^+$ CMs during postnatal growth

Neonatal mice are able to regenerate their hearts after injury during the first few days of life (20). The loss of regenerative capacity in the mouse heart is coincident with a developmental decline in the rate of CM proliferation. While the kinetics of CM proliferation in neonatal mice have been well-documented, dynamics of other cardiac cell types are not well characterized. To better define the relationship of CMs and CECs during the regenerative window of the neonatal mouse heart, we assayed CM and CEC cycling kinetics at various time points following an EdU pulse (Figure 1a-b). Cardiac sections at different developmental time points were stained for EdU incorporation along with PCM1 and Erg to specifically mark CM and CEC nuclei, respectively (17, 21-23). We developed customized image segmentation routines to objectively quantify large numbers of CECs and CMs from cardiac sections (3120 ± 734 CECs per heart and 2328 ± 751 CMs per heart, mean ± SD). Consistent with prior reports, we found the percentage of EdU$^+$ CMs to sharply decline over the first 10 days of life, with a second peak occurring at P5 (Fig. 1b,d). The increase in EdU$^+$ CMs at P5 likely coincides with a terminal round of DNA synthesis and binucleation of CMs (23, 24). EdU incorporation by CECs also declines from P1 to P10 (Fig. 1a,c) with a second peak at P7. While CM and CEC kinetics differ with regards to the timing of this second peak, the overall trends of their kinetics parallel each other. To determine the strength of this relationship, we compared rates of EdU$^+$ CECs and CMs for individual hearts and found them to be correlated ($R = 0.59$, $p = 0.0007$) (Fig. 1e). Above a threshold of ~8% EdU$^+$ CECs, each 1% increase in EdU$^+$ CMs is associated with a 1.03 ± 0.27% ($p = 0.0007$) increase in EdU$^+$ CECs.

Based on the strong temporal association of CEC and CM proliferation, we next sought to spatially relate CEC and CM cycling. Within thick sections of hearts from P4 mice pulsed with EdU, we observed numerous instances of EdU$^+$ CMs adjacent to EdU$^+$ CECs (Fig. 1f). To quantify this observation, we assigned coordinates to each CEC and CM nucleus and computed pairwise distances for every CEC and CM. We used this distance information to deconvolve overlapping microenvironments by mapping the position of every CEC relative to an EdU$^+$ CM or an EdU$^-$ CM as a function of distance, resulting in "pseudodistance maps" (Fig. 1g). When comparing the density of EdU$^+$ CECs relative to an EdU$^+$ CM or EdU$^-$ CM, we found the percentage of EdU$^+$ CECs to be enriched around EdU$^+$ CMs compared to EdU$^-$ CMs until about ~7 μm ($p = 0.04$ at 7

108 μm, two-sided Z-test) (Fig. 1g-h), providing evidence for coupled myovascular expansion during
109 physiologic growth.

110 **Coupling of myovascular growth after cryoinjury to the neonatal mouse heart**

111 Unlike other models of injury to the neonatal mouse heart, cryoinjury (CI) results in incomplete
112 or inefficient regeneration (25-28). Detailed analyses of CM proliferation kinetics after CI have
113 demonstrated that CM proliferation occurs in this model, but ostensibly at levels lower than that
114 of the uninjured neonatal heart (25, 27). Thus, we chose to evaluate myovascular expansion
115 following CI at P1 as a model of inefficient regeneration, in a regeneration-competent context. We
116 first profiled CM and CEC kinetics, considering on average of 2407 ± 891 CECs and 2153 ± 1495
117 CMs within the border zone for each heart (mean ± SD). We found that CM and CEC kinetics
118 generally follow the same trend as in the uninjured heart, with an approximately 50% decrease in
119 proliferation indices for both cell types over the first 10 days of life (Fig. 2a-d). When we compared
120 rates of CM and CEC proliferation in individual hearts, we once again noted that CM and CEC
121 proliferation rates are correlated with ~ 1% increase in the percentage of EdU^+ CECs for every
122 percent increase of EdU^+ CMs ($R = 0.54$, $p = 0.008$) (Fig. 2e). However, when we performed a
123 spatial analysis of CECs and CMs within the border zone, we did not detect enrichment of EdU^+
124 CECs in the immediate vicinity of EdU^+ CMs (Fig. 2g,h). In fact, EdU^+ CECs may even be
125 depleted around EdU^+ CMs in the border zone after CI, suggesting that CEC and CM proliferation
126 may not be efficiently coupled after CI.

127 **Association of myovascular coupling with VEGFA-VEGFR2 signaling**

128 To better understand the molecular mediators of myovascular coupling during growth and injury,
129 we performed single cell RNA-sequencing (scRNA-Seq) using border zones of P7 hearts that were
130 cryoinjured at P1. We profiled 1721 cells and identified 9 clusters of cells carrying markers of
131 CECs, CMs, fibroblasts, and inflammatory cells (Supplemental Table 1, Fig. 3a). Clusters 1, 4,
132 and 6 were notable for cells with CEC markers, such as *Fabp4, Pecam1, Erg,* and *Vegfr2*
133 (Supplemental Table 1). Compared to the other CEC clusters, cluster 4 had increased expression
134 of numerous proliferative markers, including *Ki67, Prc1, Ccna2, and Ccnb2* (Supplemental Table
135 2). A similar cluster of highly proliferative CECs has been also reported by other groups after
136 coronary ligation in neonatal and adult mice (29, 30). In the neonatal mouse heart, VEGFR2 marks
137 cardiac microvascular cells and these cells have recently been implicated in revascularization
138 following injury (17). Evaluation of sections from neonatal hearts under physiologic growth

139 conditions and after injury revealed multiple clusters of EdU^+ CMs in close proximity to EdU^+
140 $VEGFR2^+$ CECs (Fig. 3b,c), supporting a role for $VEGFR2^+$ microvascular CECs as contributing
141 to a myovascular niche of growth.

142 For many organs, parenchymal cells secrete angiogenic factors that enable matching of
143 vascular supply to organ size (31). Based on our prior work linking *vegfaa* overexpression to
144 ectopic cardiomyogenesis in the zebrafish heart, we assayed *Vegfa* expression during growth and
145 regeneration by single molecule fluorescent in situ hybridization (19). We found that under
146 physiologic growth conditions, *Vegfa* is expressed in CMs but at low levels (Supplemental Fig.
147 1a). After injury, *Vegfa* is sharply upregulated throughout the ventricle (Supplemental Fig. 1b).
148 However, based on our time course of CI responses, CEC proliferation wanes in the border zone
149 over time (Fig. 2a). To determine whether *Vegfa* levels may be contributing to CEC dynamics
150 after CI, we performed quantitative in situ hybridization of the border zone at P3 and P10 in hearts
151 cryoinjured at P1 (32). We found *Vegfa* expression to decline by ~50% from P3 to P10 in the
152 border zone (Fig. 3 d,e), paralleling kinetics of CEC cycling. Together, these data support a
153 dynamic role for myocardial VEGFA to endothelial VEGFR2 signaling as a regulator of the
154 myovascular expansion during growth and regeneration.

155 **Requirement of endothelial *Vegfr2* for CM proliferation during growth and regeneration**

156 Based on our scRNA-Seq experiments indicating that many proliferating CECs are $Vegfr2^+$, we
157 hypothesized that VEGFR2 signaling is a critical mediator of myovascular growth in the early
158 neonatal period. To conditionally delete *Vegfr2* from CECs, we crossed $Vegfr2^{flox/flox}$ mice to
159 *Cdh5-CreER*^{T2} mice to generate *Cdh5-CreER*^{T2}; $Vegfr2^{flox/flox}$ ($Vegfr2^{\Delta EC}$) and $Vegfr2^{flox/flox}$
160 ($Vegfr2^{WT}$) mice (33, 34). We verified loss of VEGFR2 from CECs by immunostaining for
161 VEGFR2 in $Vegfr2^{\Delta EC}$ mice (Supplementary Fig. 2a). Evaluation of CECs in $Vegfr2^{\Delta EC}$ mice
162 revealed fewer CECs than in $Vegfr2^{WT}$ animals and a nearly 80% reduction in CEC proliferation
163 (Fig. 4a,b). To determine how CM growth is affected by the absence of *Vegfr2* from CECs, we
164 next assayed EdU incorporation by CMs. While CM numbers were largely preserved, CM cycling
165 was also attenuated by ~ 80% in $Vegfr2^{\Delta EC}$ mice compared to $Vegfr2^{WT}$ mice (Fig. 4c,d) . We next
166 evaluated the effect of *Vegfr2* deletion from CECs on myovascular growth after cryoinjury. Similar
167 to our results during early neonatal growth, relative numbers of CECs were decreased while
168 relative CM numbers were preserved in $Vegfr2^{\Delta EC}$ hearts. We identified defects in both CEC and
169 CM incorporation of EdU after injury in $Vegfr2^{\Delta EC}$ mice (Fig. 4e-h). Specifically, we observed

170 *Vegfr2*$^{\Delta EC}$ hearts to have an almost 80% decrease in cycling CECs after injury and a 40% decrease
171 in cycling CMs. Consistent with our hypothesis, CM expansion during growth and regeneration is
172 dependent on intact *Vegfr2* in CECs.

173 **Inhibition of VEGFA limits CEC and CM proliferation**

174 Our expression data suggest a role for myocardial *Vegfa* in myovascular coupling during growth
175 and after injury (Fig. S1, 3d). To functionally test this concept, we obtained a well-described
176 synthetic antibody, B20-4.1.1 (anti-VEGFA), that binds murine VEGFA and prevents interaction
177 with its receptors (35). Treatment of neonatal mice with anti-VEGFA decreased CEC proliferation
178 by approximately 70% during early neonatal growth and by about 90% after injury indicating a
179 dependency of CEC proliferation on VEGFA (Fig. 5 a,b,e,f). Defects in CEC proliferation
180 following anti-VEGFA treatment were accompanied by decreases in the fraction of EdU^{+} CMs
181 during growth and after injury (Fig. 5 c,d,g,h), further supporting the need for myovascular
182 coupling during growth and regeneration.

183 Prior work has described a critical role for tissue hypoxia as a regulator of CM proliferation
184 in both zebrafish and mice (4, 36, 37). Remarkably, hypoxic pre-conditioning of adult mice results
185 in cardiac growth and enhanced regenerative capacity (38). Mechanistically, hypoxia decreases
186 levels of reactive oxygen species, enabling CM cell cycle-reentry (36). As the decreased
187 vascularity in *Vegfr2*$^{\Delta EC}$ mice and anti-VEGFA treated mice might be expected to result in tissue
188 hypoxia, we examined hypoxia in CMs under these conditions. Pimonidazole is a 2-nitroimidazole
189 used to identify tissue hypoxia based on its formation of stable adducts in the presence of low
190 oxygen tension (39, 40). These adducts can be detected by immunofluorescence with the intensity
191 of staining directly proportional to the level of hypoxia. We administered pimonidazole prior to
192 harvest of hearts from *Vegfr2*$^{\Delta EC}$ mice, *Vegfr2*^{WT} mice, and mice injected with anti-VEGFA or
193 vehicle. We noted an approximately 75% increase in the intensity of pimonidazole uptake by CMs
194 of *Vegfr2*$^{\Delta EC}$ mice compared to *Vegfr2*^{WT} mice and an almost 2-fold increase in mice treated with
195 anti-VEGFA compared to mice treated with vehicle (Supplemental Fig. 3). Together, these results
196 suggest that CECs are a required mediator for CM proliferation in response to tissue hypoxia.

197 **Exogenous VEGFA enhances the efficiency of innate regenerative responses.**

198 Based on the impaired spatial myovascular coupling of CECs and CMs after CI (Fig. 2g-i) and the
199 decrease of *Vegfa* in the border zone after CI (Fig. 3d), we hypothesized that increasing *Vegfa*
200 levels within the border zone might enhance the efficiency of regenerative growth following CI

201 (19). To test our hypothesis, we generated adeno-associated virus to overexpress *Vegfa* (AAV-
202 *Vegfa*) or GFP (AAV-*GFP*). We then cryoinjured mice at P1 and injected AAV-*Vegfa* or AAV-
203 *GFP* into the border zone immediately after injury (Supplemental Fig. 2b-c). Gross examination
204 of hearts injected with a resin to opacify the coronaries hearts at P21 identified increased
205 vascularity at the site of injury of AAV-*Vegfa* hearts compared to AAV-*GFP* hearts (Supplemental
206 Fig. 2c). In addition, we noted that AAV-*Vegfa* hearts had ~50% less scarring of the left ventricle
207 and better cardiac function after CI (Fig. 6 a-), all suggestive of enhanced regeneration.
208 Importantly, while CEC density was increased in animals treated with AAV-*Vegfa* (Fig. 6 e,f), this
209 was accompanied by a more than 2-fold increase of Ki67^{+} CMs in the border zone compared to
210 hearts treated with AAV-*GFP* (Fig. 6h). Finally, we evaluated sarcomere morphology and α-SMA
211 expression, two markers of CM maturity (20, 41). Compared to uninjured hearts and hearts treated
212 with AAV-*GFP*, AAV-*Vegfa* treated hearts were notable for CMs with sarcomeric staining on the
213 periphery of the cell, similar to prior descriptions of sarcomere disassembly (Supplemental Fig.
214 4a, b) (20). Also consistent with a less mature CM phenotype in AAV-*Vegfa* hearts, CMs were
215 more likely to express the dedifferentiation marker αSMA after AAV-*Vegfa* treatment
216 (Supplemental Fig. 4c-e). Together, these data indicate that exogeneous *Vegfa* in the border zone
217 can enhance regenerative responses after neonatal CI by increasing CECs, promoting CM
218 dedifferentiation and proliferation, reducing scarring, and restoring ventricular function.

219 **Association of genetically predicted VEGFA levels with myocardial mass in human**

220 Our results after CI in neonatal mice suggest exogenous *Vegfa* could be used
221 therapeutically to promote cardiac growth and regeneration. Indeed, exogenous *Vegfa* has been
222 shown to stimulate cardiac repair after experimental infarction many times in adult mammals, even
223 prompting several human clinical trials in patients with ischemic heart disease (42-47). However,
224 clinical trials have largely failed to improve outcomes, possibly because of inefficient delivery
225 methods that did not sufficiently raise local *Vegfa* levels (48, 49).

226 Based on its potential as a regenerative factor, we sought to conceptually determine
227 whether VEGFA might regulate cardiac growth in humans using Mendelian randomization (MR).
228 MR is an epidemiologic technique that uses genetic variation to infer causality from observational
229 studies (50-52). Traditional observational studies that associate factors with an outcome are prone
230 to confounding and cannot differentiate causation from reverse causation. However, because

231 innate factors tend to be independent of confounding variables, MR studies are used to point
232 towards causality, and have been used to successfully predict the results of clinical trials (53).
233 We performed two-sample *cis* Mendelian randomization (MR) analysis with genetically
234 predicted circulating VEGFA concentration as the exposure variable and traits of cardiac structure
235 and function as the outcomes (Fig. 7) (54). Under this framework, genetic variants acting in *cis*
236 that associate with protein abundance (protein quantitative trait loci, pQTL) are used as
237 instrumental variables to estimate the unconfounded causal effects of the protein on the outcomes
238 of interest (Fig. 7a). Genetic variants within the VEGFA gene region were selected from genetic
239 association summary statistics from a genome-wide association study (GWAS) of directly
240 measured circulating VEGFA concentration in over 30,000 individuals (Fig. 7b, Supplemental
241 Table 3) (55). Variant association statistics for six parameters of left ventricular (LV) structure and
242 function were then extracted from a GWAS of cardiac magnetic resonance imaging measures in
243 the UK Biobank (56). A summary of the GWAS is presented in Supplemental Table 4. We applied
244 these instruments, using a two-sample MR model that accounts for partial correlation between
245 instruments, to estimate the effect of genetically predicted circulating VEGFA on LV phenotypes
246 (52). We did not detect a link between genetically predicted VEGFA levels and left ventricular
247 volumes or ejection fraction but found that higher genetically predicted VEGFA levels resulted in
248 increased LV mass (at type I error rate = 0.05 / 6), (Fig. 7c,d). In total, we found an estimated 1.02
249 gram (95% CI = 0.33-1.70 gram, p = 0.004) increase in LVM per doubling of the circulating
250 VEGFA concentration. Because there is a lack of consensus on how genetic instruments are
251 selected and MR modeling, we performed a sensitivity analysis. Across 120 separate analyses
252 with varying thresholds for instrument selection and four different MR modeling approaches, 119
253 of these analyses indicate that higher levels of VEGFA are robustly associated with higher LVM
254 (Fig 7e). These results are consistent with the hypothesis that VEGFA promotes cardiac growth in
255 humans and support a possible therapeutic role for VEGFA.
256
257 **DISCUSSION**
258 We profiled CEC and CM dynamics to determine that CEC and CM cycling are
259 spatiotemporally coupled in the neonatal mouse heart. Uncoupling CECs from CMs, by deletion
260 of *Vegfr2* from CECs or with an anti-VEGFA antibody, dramatically decreases CM proliferation
261 (Figs 4 and 5). Conversely, improving CEC and CM coupling after CI by increasing local *Vegfa*

262 increases regeneration after CI (Fig. 6). Analogously, myocardial mass of the human heart
263 increases with higher VEGFA levels (Fig. 7). Together, our work demonstrates that the efficiency
264 of cardiac growth is dependent upon myovascular interactions, a finding with strong translational
265 relevance. Approximately 50% of patients with systolic heart failure have flow-limiting coronary
266 artery disease (57). Even in so-called "non-ischemic" cardiomyopathies, cardiac perfusion is
267 impaired due to microvascular disease and capillary rarefaction (58-62). Thus, as methods to
268 promote proliferation of adult mammalian CMs move towards therapeutics, mechanical or
269 molecular revascularization approaches may be a required adjunct for these approaches to be
270 maximally efficacious.

271 A key concept suggested by our work is that of growth niches, in which cycling CECs
272 establish inductive microenvironments to promote CM proliferation (Fig. 1, 2). We find that
273 cycling CECs are statistically enriched within 7 μm, or 1-2 cell lengths, of cycling CMs during
274 physiologic growth. Because we used pairwise comparisons of CEC and CM distances to
275 deconvolve overlapping niches, our spatial analysis likely underestimates the expanse of the niche
276 surrounding cycling CMs. However, our results are remarkably well-aligned with reported
277 increases of CM proliferation within 3 cell lengths of sprouting angiogenesis in cultured fetal heart
278 sections (63). Niches for CM expansion in the postnatal mammalian heart have been previously
279 identified around hypoxic regions, with hypoxia even being able to induce CM proliferation in the
280 adult mouse heart (4, 38). Mechanistically, hypoxia exerts its effect on CM proliferation cell
281 autonomously, by modulating reactive oxygen species and the DNA damage response (36). Our
282 work suggests another element to the phenomenon of hypoxia-induced CM proliferation. We were
283 able to induce hypoxia in the neonatal heart through two different approaches, genetic deletion of
284 *Vegfr2* from CECs and with an anti-VEGFA antibody (Supplemental Fig. 3). However, even
285 though hypoxia would be predicted to increase CM proliferation, we observed decreased CM
286 cycling in these models. Thus, hypoxia mediated CM expansion is likely to involve both CM-
287 specific effects but to also depend on CECs within the hypoxic niche. While hypoxia may be one
288 approach to stimulate heart regeneration, therapeutic hypoxia for patients with heart failure may
289 be challenging. A better understanding of the signaling milieu of the hypoxic niche could lead to
290 alternate approaches for stimulating hypoxia-mediated regeneration.

291 Because depletion of CECs, either through deletion of *Vegfr2* from CECs or by
292 administration of anti-VEGFA, leads to defects in CM proliferation, our work demonstrates that

293 CECs promote CM cycling (Fig. 5, 6). Mechanistically, CEC expansion may simply lead to new
294 conduits for growth factors or other cell types that promote cardiac growth. However, multiple
295 lines of evidence also point to a direct role for CECs to influence CM proliferation through
296 angiocrines. Indeed, recent work in zebrafish and neonatal mice support this concept. In zebrafish,
297 inhibition of Notch in CECs results in reduced secretion of Wnt inhibitors that influence CM
298 proliferation (64). More directly, deletion of *Igf2* from CECs in developing mice abrogates CM
299 proliferation after neonatal cardiac injury (65). Interestingly, deletion of *Igf2* from CECs does not
300 affect physiologic CM cycling, raising the intriguing possibility that different angiocrines
301 modulate myocardial expansion during physiologic growth and after injury. Finally, different CEC
302 subsets may contribute different sets of angiocrines, as recent work suggests that *Reln* from
303 lymphatic endothelial cells has direct effects on CM proliferation (13). Future work to identify the
304 complement of angiocrines that instruct CM proliferation in different developmental and injury
305 contexts is needed.

306 Our work also suggests that restoring myovascular coupling can enhance regenerative
307 capacity. Unlike physiologic growth, CEC cycling is not enriched around cycling CMs in the
308 border zone after CI, a model of incomplete regeneration. Functionally increasing CEC density
309 through overexpression of the master angiokine *Vegfa* enhances CM cycling and reduces scarring
310 after CI, both signs of enhanced regeneration (Fig. 6). Taken together with our prior work showing
311 that *vegfaa* overexpression can induce ectopic heart regeneration in zebrafish, exogenous *Vegfa*
312 may be one approach to augment regeneration. Indeed, our MR study indicates that VEGFA levels
313 are causally linked to human myocardial mass and predict that more VEGFA can increase human
314 cardiac growth (Figure 7). Several clinical trials of *Vegfa* are now underway to revisit whether
315 exogenous VEGFA can be used therapeutically to treat human cardiovascular disease
316 (NCT03409627, NCT03370887, and NCT04125732). Compared to prior clinical trials, these
317 studies utilize newer delivery methods such as modified RNAs, newer generation viral vectors,
318 and more efficient plasmid delivery systems. Based partly on our findings, we would expect that
319 markers of increased CECs, such as improvements in myocardial perfusion, will predict VEGFA-
320 based treatment effects on cardiac mass and function.

321 We acknowledge several limitations to our work. First, although we focus on the coupling
322 of CECs and CMs during growth and regeneration, additional cell types also regulate cardiac
323 growth and are likely to be present within niches. Defining niche constituents may be critical to

324 efficiently instruct cardiac growth. Second, while we demonstrate a critical role of VEGFA-
325 VEGFR2 signaling to coordinate CEC and CM expansion, VEGFR2 broadly marks the cardiac
326 microvasculature. Future work to refine which microvascular cells instruct CM cycling could
327 enable more targeted regenerative approaches via cell transplantation or specific signaling cues.
328 Finally, while our MR studies point to a therapeutic benefit to using VEGFA to stimulate cardiac
329 growth, our MR studies model a lifetime of exposure to VEGFA and do not have the resolution to
330 confirm that increased myocardial mass is the result of CM expansion. Additional work to
331 determine whether VEGFA promotes cardiac growth across developmental stages and to directly
332 link VEGFA to human CM proliferation in vivo are needed to establish VEGFA as a bona fide
333 regenerative factor in humans.
334 In summary, here, we present work showing that coordinated growth of CECs and CMs guides
335 postnatal cardiac growth and regeneration. We speculate that a better understanding of the
336 signaling milieu within a myovascular niche can inform approaches for heart regeneration.
337

338 **METHODS**

339 **Mice and Neonatal Cryoinjuries**

340 CD-1 mice (Charles River Labs, Morrisville, NC) were used for profiling myovascular kinetics
341 during growth and regeneration. CD-1 mice were also used for anti-VEGFA antibody and AAV
342 experiments. *Cdh5-CreER*^{T2} and *Vegfr2*$^{flox/flox}$ strains have been previously described (33, 34).
343 *Cdh5-CreER*^{T2}; *Vegfr2*$^{flox/flox}$ and *Vegfr2*$^{flox/flox}$ mice were treated with 100 mg of tamoxifen
344 intraperitoneally at P0 and P1. Complete recombination was verified by immunostaining for
345 VEGFR2 (Supplementary Fig. 2). For EdU incorporation studies, 0.5 mg EdU was given
346 intraperitoneally 4 hours prior to tissue harvest. Cryoinjuries were performed on P1 pups as
347 previously described (25, 28).
348 The number of animals used in these studies is specified in the figure legends. For mouse
349 experiments, we included animals 1) confirmed to have *Vegfr2* deletion by immunostaining for
350 VEGFR2; 2) animals with weight loss after anti-VEGFA treatment; or 3) animals confirmed to
351 have *Vegfa* overexpression by in situ hybridization after injection with AAV-*Vegfa*. For assays
352 without computational scoring, readers were blinded to experimental groups. All protocols were
353 approved by the Institutional Animal Care and Use Committee at Duke University.

354 **Histology and Immunostaining**

355 At the time of tissue harvest, hearts were perfused with KCl and then 4% PFA. Hearts were then
356 immersed in 30% sucrose overnight and embedded in Tissue Freezing Media for cryosectioning.
357 Cryosections were blocked with PBST (PBS with 0.1% Tween-20) containing 10%
358 newborn calf serum and 1% DMSO and incubated overnight with primary antibodies at 4ºC.
359 Cryosections were then washed with PBST and incubated with secondary antibodies and DAPI
360 (100 ng/ml). For EdU detection, cryosections were incubated in EdU staining solution (100 mM
361 Tris-HCl, 1 mM $CuSO_4$, 10 mM Azide, and 50 mM ascorbic acid in PBS) for 10 minutes. Primary
362 antibodies used for this study included: anti-PCM1 (Sigma, HPA023370, 1:100); anti-PCM1
363 (Santa Cruz, sc-398365, 1:100); anti-Erg (Abcam, ab92513, 1:25); anti-CD31
364 (BDBioscience, 553370, 1:100), anti-VEGFR2 (BDBioscience, 555307, 1:100), anti-Ki67
365 (ThermoFisher, 4-5698-82, 1:100), anti-Actinin (Cell Signaling, 6487P, 1:100), anti-Tnnt (DSHB
366 CT3, 1:25) αSMA (Abcam, ab5694, 1:200). Secondary antibodies and azides were conjugated to
367 Alexa-488, Alexa-594, or Alexa-633 (Invitrogen). To label CM nuclei, cryosections underwent
368 heat induced epitope retrieval with citrate buffer prior to immunostaining. Stained slides were
369 imaged on a Zeiss AxioImager M1 epifluorescent microscope, a Zeiss CSU-X1 spinning disk
370 confocal microscope, or a Zeiss LSM 510 confocal microscope. For physiologic growth
371 experiments, 9 -16 non-overlapping images (40X) of the left ventricle were obtained for each
372 section. For CI experiments, the border zone was defined as the entire region within 1-2 40X fields
373 of view along the entirety of the injury plane. For each heart, the 3 largest sections were imaged.
374 **Quantification of CM and CEC Proliferation**
375 We developed several customized image segmentation pipelines using CellProfiler and Ilastik for
376 automated scoring EdU^+ CECs and CMs (66, 67). For CEC quantification, grayscale images for
377 each channel were processed with rolling-ball background subtraction and used as input into a
378 CellProfiler routine that 1) identified Erg^+ nuclei based on Erg staining and DAPI intensity; 2)
379 identified EdU^+ nuclei based on EdU staining and DAPI staining; and 3) identified EdU^+ Erg^+
380 nuclei based on the presence of an EdU object within an Erg object.
381 For CMs, grayscale images from individual channels were obtained using a Zeiss CSU-X1
382 spinning disk confocal microscope. Images were pre-processed to generate 32-bit grayscale
383 images and to create a set of images with merged PCM1 and DAPI channels. The DAPI image
384 and the merged PCM1-DAPI images were then input into machine learning routines to generate
385 probability maps for $DAPI^+$ nuclei and $PCM1^+/DAPI^+$ nuclei, using Ilastik. Machine learning

386 algorithms were trained using images from our physiologic growth experiments. Probability maps
387 and grayscale images were used as input for a CellProfiler pipeline that 1) identified nuclei based
388 on a DAPI probability map; 2) filtered nuclei for CMs based on the mean $PCM1^+/DAPI^+$ pixel
389 probability; 3) identified EdU^+ nuclei based on EdU staining and DAPI staining; and 4) identified
390 EdU+ CM nuclei based on the presence of an EdU object within a CM nucleus. CellProfiler output
391 data was tabulated using the dplyr package in R (68).

392 **Proximity mapping**

393 For proximity mapping, z-stack images of P4 hearts were obtained using a Zeiss LSM 510 confocal
394 microscope. CM and CEC nuclei were segmented using the Spots tool along with manual
395 refinement, assigned coordinates, and categorized as EdU^+ or EdU^- using Imaris (Bitplane AG,
396 Zurich, Switzerland). Coordinate files were then used to determine the pairwise distance of each
397 CM and each CEC nucleus. Distances were used to compute the density of EdU^+ CECs as a
398 function of distance from each $PCM1^+$ nucleus using the dplyr and plotly packages in R (68, 69).

399 **In situ hybridization**

400 RNAscope Probe - Mm-Vegfa-O2 (Lot 16197A), with predicted reactivity against all known
401 murine *Vegfa* variants, was hybridized against cryosections using the manufacturer's protocol
402 (Advanced Cell Diagnostics, Hayward, CA). Images of sections were quantified using a
403 CellProfiler routine adapted from Erben et al (32). Briefly, the DAPI channel was used to identify
404 nuclei objects and the number of *Vegfa* spots adjacent to each nucleus was counted.

405 **Single Cell RNA Sequencing and Analysis**

406 The left ventricles of cryoinjured hearts were collected at P7. The apical third of the LV that
407 contained the injured area was then dissociated into single cells. Single cells were then captured
408 into droplets using microfluidics followed by preparation of single cell cDNA libraries as
409 previously described (70). Samples were sequenced on a single lane of an Illumina HiSeq.
410 Sequencing reads were mapped to Ensembl release NCBIM37.67. Aligned reads were binned and
411 collapsed onto cellular barcodes using the Drop-seq pipeline v1.13.3
412 (http://mccarrolllab.com/dropseq), resulting in a raw digital expression matrix containing the count
413 of unique UMIs for each gene in each cell (71).

414 Expression analysis was performed by the Duke Bioinformatics Shared Resource, using
415 the Seurat package (v2.2.0) in R/Bioconductor **(72)**. Cells with gene counts over 4,000 or less than
416 200 were removed. Genes expressed in less than three cells were also removed. To avoid over-

417 filtering CMs, we did not filter cells based on high expression of mitochondrial genes. Gene
418 expression, for 1721 cells across 12754 genes, was normalized by scaling by the total number of
419 transcripts, multiplying by 10,000, and log transformation. Unwanted sources of variation were
420 adjusted for by regression on the number of detected UMIs using the *ScaleData* function. We used
421 the JackStraw method to determine the number of statistically significant principal components
422 (PCs). The *FindClusters* function was used to identify cellular clusters, using the 20 significant
423 PCs and a 0.6 resolution. We used the t-SNE method to visualize cells across 20 PCs in two
424 dimensions. To identify cell types, we used the *FindAllMarkers* function. Parameters were set to
425 test all genes, expressed in at least 10% of the cells in each cluster, for differential expression.

426 **Anti-VEGFA Antibody Treatment**

427 Anti-VEGFA antibody (B20-4.1.1) was a kind gift from Genentech (San Francisco, CA). Neonatal
428 mice were injected with 5 mg/g of anti-VEGFA or vehicle at P0 and P4. Adequate injection of
429 anti-VEGFA was confirmed by significant weight loss compared to control animals at the time of
430 tissue harvest.

431 **Determination of Hypoxia**

432 Mice were given 60 mg/g pimonidazole (Hypoxyprobe, HP3-100kit) intraperitoneally 1.5 hours
433 prior to tissue harvest. Tissues sections were stained with an anti-pimonidazole antibody
434 (Hypoxyprobe, HP3-100kit, 1:100) and an antibody against a-actinin. For each heart, 9 images of
435 the left ventricle for 3 separate cardiac sections were obtained using an AxioImager M1
436 microscope. Images were quantified using a CellProfiler routine to 1) create an image mask based
437 on the a-actinin stain and 2) determine the mean intensity of anti-pimonidazole stain.

438 **AAV Generation and Treatment**

439 AAV encoding *Vegfa-164* under the control of a CMV promoter was generated by PCR amplifying
440 the *Vegf164* isoform of *Vegfa* from a mouse endothelial cDNA library and cloning this fragment
441 into the pTR2-eGFP with replacement of *EGFP* (73). AAV, serotype 9, was generated through the
442 Duke Viral Vector core. AAV virus encoding *GFP* under the control of a CMV promoter was
443 obtained from the Duke Viral Vector Core. For intracardiac injections, 12 μl of AAV at
444 $1x10^9$ vg/ml was injected circumferentially around the injured area immediately after CI
445 (Supplemental Fig. 2b).

446 **Coronary vessel labeling**

447 The coronary vasculature was visualized by injection of a low viscosity polyurethane resin
448 (PU4ii, VasQTec) into the apex of the left ventricle (74). Whole mount images were obtained
449 using a stereoscope.

450 **Scar Assessment**

451 P21 hearts were serially sectioned from base to apex and stained with acid fuchsin orange G, as
452 previously described (75). Stained slides were scanned with a Leica Aperio Digital Pathology
453 Slide Scanner. Scar area as a percentage of the left ventricle was scored by a blinded reader. The
454 average scar percentage across the 5 largest sections was determined for each heart.

455 **Echocardiography**

456 Fractional shortening was determined by echocardiography using the Duke Cardiovascular
457 Physiology Core. Images were analyzed by three blinded readers and an averaged reading is
458 reported.

459 **Mendelian Randomization to Determine Effects of Circulating VEGFA Levels on Human**
460 **Cardiac Structure**

461 Two-sample MR analysis was performed using summary statistics from GWAS of circulating
462 protein level measured with Olink proximity-extension assay in 30,931 individuals of European
463 ancestries and GWAS of cardiac MRI – derived left ventricular phenotypes in 16,923 UK Biobank
464 participants (Supplementary Table 4) (55, 56). To represent effect in the original unit of
465 measurements, the standardized estimates from both GWAS were back-transformed by
466 multiplying the MR effect estimate with the estimated standard deviation of the traits. MR
467 instruments for VEGFA were selected from variants that 1) are available in both GWAS, 2) located
468 within the 200 kilobases flanking region from the genomic coordinate of *VEGFA* gene; 3) have a
469 MAF > 0.01; 4) have a *P*-value for association with circulating VEGFA level < $1x10^{-4}$; and 5) are
470 LD-clumped to an r^2 threshold of 0.4 using *plink* with --clump option (76). Mendelian
471 randomization analysis was performed using an inverse-variance weighted model accounting for
472 correlation between instruments, implemented in the *MendelianRandomization* R package (77,
473 78). Correlation between instruments were estimated from a random sample of 10,000 UK
474 Biobank participants of European ancestries (79).

475 To test the robustness of the cis-MR analysis, a series of sensitivity analyses were
476 performed by varying parameters for instrument selection and MR models. For instrument
477 selection, LD clumping was performed using five different r^2 thresholds (0.05, 0.1, 0.2, 0.4, and

0.6) and six different *P*-value thresholds for association with circulating VEGFA level (no threshold), $1e^{-2}$, $1e^{-3}$, $1e^{-4}$, $1e^{-5}$, and $5e^{-8}$). Four different MR models were also tested for each instrument set (inverse-variance weighted, MR-Egger, Principal component MR with 90% variance explained, and Principal component MR with 99% variance explained) (80, 81). To account for correlation between instruments, we implemented the method proposed by Burgess *et al.* using an instrument correlation model derived from genotype data of a random subset of 10,000 UK Biobank participants of European ancestry (77).

Statistics

All means are presented as mean ± SEM and proportions as proportion ± 95% confidence interval (95% CI). Statistical analysis between two groups was performed using a two-tailed unpaired t-test test. Pairwise comparisons between multiple groups were performed using a two-tailed unpaired t-test test with correction for multiple testing using Holm's method. A $p < 0.05$ was set as an *a priori* threshold for significance. Statistical analysis and plots were generated in R using the dplyr, ggpubr, and ggplot2 packages (68, 82, 83). For each experiment, individual data points are presented in the plot and the sample size is specified in the figure legend.

Study approval

All animal protocols were approved by the Institutional Animal Care and Use Committee at Duke University.

Acknowledgments: We thank Ken Poss, Nenad Bursac, Doug Marchuk, and Howard Rockman for comments and discussion. We would like to thank Dr. Helene Fradin Kirshner from the Duke Bioinformatics Shared Resource for assistance with the analysis of scRNA-seq data.

Author contributions:

Conceptualization: RK

Methodology: RK, RTL, PRT, SHS

Investigation: PD, AK, AH, KB, AP, MCT, YK, TM, CK, RTL, RK

Visualization: PD, AK, AH, RTL, RK

Funding acquisition: RK, RTL

Project administration: PD, RTL, RK

Supervision: RK, RTL

Writing – original draft: PD, RK

Writing – review & editing: PD, AH, SHS, CDK, RTL, RK.

Sources of Funding:

National Institutes of Health grant R03 HL144812 (RK)

Duke University Strong Start Physician Scientist Award (RK),

Mandel Foundation Seed Grant (RK)

Walker P. Inman Endowment (RK)

UK Research and Innovation Rutherford Fellowship MR/S003754/1 hosted by Health Data Research UK (RTL)

BigData@Heart Consortium funded by the Innovative Medicines Initiative-2 Joint Undertaking grant 116074 (RTL)

National Institute for Health Research University College London Hospitals Biomedical Research Centre (RTL)

Disclosures: None

524 **References**

525 1. Wagers AJ. The stem cell niche in regenerative medicine. *Cell Stem Cell.*
526 2012;10(4):362-9.
527 2. Lane SW, Williams DA, and Watt FM. Modulating the stem cell niche for tissue
528 regeneration. *Nat Biotechnol.* 2014;32(8):795-803.
529 3. Fuchs E, and Blau HM. Tissue Stem Cells: Architects of Their Niches. *Cell Stem Cell.*
530 2020;27(4):532-56.
531 4. Kimura W, Xiao F, Canseco DC, Muralidhar S, Thet S, Zhang HM, et al. Hypoxia fate
532 mapping identifies cycling cardiomyocytes in the adult heart. *Nature.*
533 2015;523(7559):226-30.
534 5. Poss KD, Wilson LG, and Keating MT. Heart regeneration in zebrafish. *Science.*
535 2002;298(5601):2188-90.
536 6. Kikuchi K, Holdway JE, Werdich AA, Anderson RM, Fang Y, Egnaczyk GF, et al.
537 Primary contribution to zebrafish heart regeneration by gata4(+) cardiomyocytes. *Nature.*
538 2010;464(7288):601-5.
539 7. Oberpriller J, and Oberpriller JC. Mitosis in adult newt ventricle. *J Cell Biol.*
540 1971;49(2):560-3.
541 8. Jopling C, Sleep E, Raya M, Marti M, Raya A, and Izpisua Belmonte JC. Zebrafish heart
542 regeneration occurs by cardiomyocyte dedifferentiation and proliferation. *Nature.*
543 2010;464(7288):606-9.
544 9. Wang J, Cao J, Dickson AL, and Poss KD. Epicardial regeneration is guided by cardiac
545 outflow tract and Hedgehog signalling. *Nature.* 2015;522(7555):226-30.
546 10. Mahmoud AI, O'Meara CC, Gemberling M, Zhao L, Bryant DM, Zheng R, et al. Nerves
547 Regulate Cardiomyocyte Proliferation and Heart Regeneration. *Dev Cell.*
548 2015;34(4):387-99.
549 11. Aurora AB, Porrello ER, Tan W, Mahmoud AI, Hill JA, Bassel-Duby R, et al.
550 Macrophages are required for neonatal heart regeneration. *J Clin Invest.*
551 2014;124(3):1382-92.
552 12. Fernandez CE, Bakovic M, and Karra R. Endothelial Contributions to Zebrafish Heart
553 Regeneration. *J Cardiovasc Dev Dis.* 2018;5(4).
554 13. Liu X, De la Cruz E, Gu X, Balint L, Oxendine-Burns M, Terrones T, et al.
555 Lymphoangiocrine signals promote cardiac growth and repair. *Nature.* 2020.
556 14. Marin-Juez R, Marass M, Gauvrit S, Rossi A, Lai SL, Materna SC, et al. Fast
557 revascularization of the injured area is essential to support zebrafish heart regeneration.
558 *Proc Natl Acad Sci U S A.* 2016;113(40):11237-42.
559 15. Fan Q, Mao H, Angelini A, Coarfa C, Robertson MJ, Lagor WR, et al. Depletion of
560 Endothelial Prolyl Hydroxylase Domain Protein 2 and 3 Promotes Cardiomyocyte
561 Proliferation and Prevents Ventricular Failure Induced by Myocardial Infarction.
562 *Circulation.* 2019;140(5):440-2.
563 16. Marin-Juez R, El-Sammak H, Helker CSM, Kamezaki A, Mullapuli ST, Bibli SI, et al.
564 Coronary Revascularization During Heart Regeneration Is Regulated by Epicardial and
565 Endocardial Cues and Forms a Scaffold for Cardiomyocyte Repopulation. *Dev Cell.*
566 2019;51(4):503-15 e4.
567 17. Das S, Goldstone AB, Wang H, Farry J, D'Amato G, Paulsen MJ, et al. A Unique
568 Collateral Artery Development Program Promotes Neonatal Heart Regeneration. *Cell.*
569 2019;176(5):1128-42 e18.

570 18. Zhao L, Borikova AL, Ben-Yair R, Guner-Ataman B, MacRae CA, Lee RT, et al. Notch
571 signaling regulates cardiomyocyte proliferation during zebrafish heart regeneration. *Proc*
572 *Natl Acad Sci U S A.* 2014;111(4):1403-8.
573 19. Karra R, Foglia MJ, Choi WY, Belliveau C, DeBenedittis P, and Poss KD. Vegfaa
574 instructs cardiac muscle hyperplasia in adult zebrafish. *Proc Natl Acad Sci U S A.*
575 2018;115(35):8805-10.
576 20. Porrello ER, Mahmoud AI, Simpson E, Hill JA, Richardson JA, Olson EN, et al.
577 Transient regenerative potential of the neonatal mouse heart. *Science.*
578 2011;331(6020):1078-80.
579 21. Bergmann O, Zdunek S, Alkass K, Druid H, Bernard S, and Frisen J. Identification of
580 cardiomyocyte nuclei and assessment of ploidy for the analysis of cell turnover. *Exp Cell*
581 *Res.* 2011;317(2):188-94.
582 22. Bergmann O, Bhardwaj RD, Bernard S, Zdunek S, Barnabe-Heider F, Walsh S, et al.
583 Evidence for cardiomyocyte renewal in humans. *Science.* 2009;324(5923):98-102.
584 23. Alkass K, Panula J, Westman M, Wu T-D, Guerquin-Kern J-L, and Bergmann O. No
585 evidence for cardiomyocyte number expansion in preadolescent mice. *Cell.*
586 2015;163(4):1026-36.
587 24. Soonpaa MH, Kim KK, Pajak L, Franklin M, and Field LJ. Cardiomyocyte DNA
588 synthesis and binucleation during murine development. *American Journal of Physiology-*
589 *Heart and Circulatory Physiology.* 1996;271(5):H2183-H9.
590 25. Polizzotti BD, Ganapathy B, Walsh S, Choudhury S, Ammanamanchi N, Bennett DG, et
591 al. Neuregulin stimulation of cardiomyocyte regeneration in mice and human
592 myocardium reveals a therapeutic window. *Sci Transl Med.* 2015;7(281):281ra45.
593 26. Polizzotti BD, Ganapathy B, Haubner BJ, Penninger JM, and Kuhn B. A cryoinjury
594 model in neonatal mice for cardiac translational and regeneration research. *Nat Protoc.*
595 2016;11(3):542-52.
596 27. Darehzereshki A, Rubin N, Gamba L, Kim J, Fraser J, Huang Y, et al. Differential
597 regenerative capacity of neonatal mouse hearts after cryoinjury. *Dev Biol.*
598 2015;399(1):91-9.
599 28. Bakovic M, Thakkar D, DeBenedittis P, Chong DC, Thomas MC, Iversen ES, et al.
600 Clonal Analysis of the Neonatal Mouse Heart using Nearest Neighbor Modeling. *Journal*
601 *of Visualized Experiments: Jove.* 2020(162).
602 29. Wang Z, Cui M, Shah AM, Tan W, Liu N, Bassel-Duby R, et al. Cell-Type-Specific
603 Gene Regulatory Networks Underlying Murine Neonatal Heart Regeneration at Single-
604 Cell Resolution. *Cell Rep.* 2020;33(10):108472.
605 30. Wu X, Reboll MR, Korf-Klingebiel M, and Wollert KC. Angiogenesis After Acute
606 Myocardial Infarction. *Cardiovasc Res.* 2020.
607 31. Rafii S, Butler JM, and Ding BS. Angiocrine functions of organ-specific endothelial
608 cells. *Nature.* 2016;529(7586):316-25.
609 32. Erben L, and Buonanno A. Detection and quantification of multiple RNA sequences
610 using emerging ultrasensitive fluorescent in situ hybridization techniques. *Current*
611 *protocols in neuroscience.* 2019;87(1):e63.
612 33. Hooper AT, Butler JM, Nolan DJ, Kranz A, Iida K, Kobayashi M, et al. Engraftment and
613 reconstitution of hematopoiesis is dependent on VEGFR2-mediated regeneration of
614 sinusoidal endothelial cells. *Cell Stem Cell.* 2009;4(3):263-74.

615 34. Sorensen I, Adams RH, and Gossler A. DLL1-mediated Notch activation regulates
616 endothelial identity in mouse fetal arteries. *Blood.* 2009;113(22):5680-8.
617 35. Liang W-C, Wu X, Peale FV, Lee CV, Meng YG, Gutierrez J, et al. Cross-species
618 vascular endothelial growth factor (VEGF)-blocking antibodies completely inhibit the
619 growth of human tumor xenografts and measure the contribution of stromal VEGF.
620 *Journal of Biological Chemistry.* 2006;281(2):951-61.
621 36. Puente BN, Kimura W, Muralidhar SA, Moon J, Amatruda JF, Phelps KL, et al. The
622 oxygen-rich postnatal environment induces cardiomyocyte cell-cycle arrest through DNA
623 damage response. *Cell.* 2014;157(3):565-79.
624 37. Jopling C, Suñé G, Faucherre A, Fabregat C, and Izpisua Belmonte JC. Hypoxia induces
625 myocardial regeneration in zebrafish. *Circulation.* 2012;126(25):3017-27.
626 38. Nakada Y, Canseco DC, Thet S, Abdisalaam S, Asaithamby A, Santos CX, et al.
627 Hypoxia induces heart regeneration in adult mice. *Nature.* 2017;541(7636):222-7.
628 39. Raleigh JA, Calkins-Adams DP, Rinker LH, Ballenger CA, Weissler MC, Fowler WC,
629 Jr., et al. Hypoxia and vascular endothelial growth factor expression in human squamous
630 cell carcinomas using pimonidazole as a hypoxia marker. *Cancer Res.* 1998;58(17):3765-
631 8.
632 40. Miller G, Best M, Franko A, Koch C, and Raleigh J. Quantitation of hypoxia in
633 multicellular spheroids by video image analysis. *International Journal of Radiation*
634 *Oncology* Biology* Physics.* 1989;16(4):949-52.
635 41. Chen Y, Luttmann FF, Schoger E, Scholer HR, Zelarayan LC, Kim KP, et al. Reversible
636 reprogramming of cardiomyocytes to a fetal state drives heart regeneration in mice.
637 *Science.* 2021;373(6562):1537-40.
638 42. Zangi L, Lui KO, von Gise A, Ma Q, Ebina W, Ptaszek LM, et al. Modified mRNA
639 directs the fate of heart progenitor cells and induces vascular regeneration after
640 myocardial infarction. *Nat Biotechnol.* 2013;31(10):898-907.
641 43. Carlsson L, Clarke JC, Yen C, Gregoire F, Albery T, Billger M, et al. Biocompatible,
642 purified VEGF-A mRNA improves cardiac function after intracardiac injection 1 week
643 post-myocardial infarction in swine. *Molecular Therapy-Methods & Clinical*
644 *Development.* 2018;9:330-46.
645 44. Ferrarini M, Arsic N, Recchia FA, Zentilin L, Zacchigna S, Xu X, et al. Adeno-
646 associated virus-mediated transduction of VEGF165 improves cardiac tissue viability and
647 functional recovery after permanent coronary occlusion in conscious dogs. *Circulation*
648 *research.* 2006;98(7):954-61.
649 45. Lin YD, Luo CY, Hu YN, Yeh ML, Hsueh YC, Chang MY, et al. Instructive nanofiber
650 scaffolds with VEGF create a microenvironment for arteriogenesis and cardiac repair. *Sci*
651 *Transl Med.* 2012;4(146):146ra09.
652 46. Pearlman JD, Hibberd MG, Chuang ML, Harada K, Lopez JJ, Gladstone SR, et al.
653 Magnetic resonance mapping demonstrates benefits of VEGF–induced myocardial
654 angiogenesis. *Nature medicine.* 1995;1(10):1085-9.
655 47. Janavel GV, Crottogini A, Meckert PC, Cuniberti L, Mele A, Papouchado M, et al.
656 Plasmid-mediated VEGF gene transfer induces cardiomyogenesis and reduces
657 myocardial infarct size in sheep. *Gene therapy.* 2006;13(15):1133-42.
658 48. Taimeh Z, Loughran J, Birks EJ, and Bolli R. Vascular endothelial growth factor in heart
659 failure. *Nat Rev Cardiol.* 2013;10(9):519-30.

660 49. Oh JG, and Ishikawa K. Recent highlights and advances in cardiac gene therapy. *Discov*
661 *Med.* 2019;28(155):229-35.
662 50. Gray R, and Wheatley K. How to avoid bias when comparing bone marrow
663 transplantation with chemotherapy. *Bone marrow transplantation.* 1991;7:9-12.
664 51. Emdin CA, Khera AV, and Kathiresan S. Mendelian Randomization. *JAMA.*
665 2017;318(19):1925-6.
666 52. Schmidt AF, Finan C, Gordillo-Maranon M, Asselbergs FW, Freitag DF, Patel RS, et al.
667 Genetic drug target validation using Mendelian randomisation. *Nat Commun.*
668 2020;11(1):3255.
669 53. Ference BA. How to use Mendelian randomization to anticipate the results of randomized
670 trials. *European Heart Journal.* 2017;39(5):360-2.
671 54. Davey Smith G, and Hemani G. Mendelian randomization: genetic anchors for causal
672 inference in epidemiological studies. *Hum Mol Genet.* 2014;23(R1):R89-98.
673 55. Folkersen L, Gustafsson S, Wang Q, Hansen DH, Hedman AK, Schork A, et al. Genomic
674 and drug target evaluation of 90 cardiovascular proteins in 30,931 individuals. *Nat*
675 *Metab.* 2020;2(10):1135-48.
676 56. Aung N, Vargas JD, Yang C, Cabrera CP, Warren HR, Fung K, et al. Genome-Wide
677 Analysis of Left Ventricular Image-Derived Phenotypes Identifies Fourteen Loci
678 Associated With Cardiac Morphogenesis and Heart Failure Development. *Circulation.*
679 2019;140(16):1318-30.
680 57. Benjamin EJ, Virani SS, Callaway CW, Chamberlain AM, Chang AR, Cheng S, et al.
681 Heart disease and stroke statistics—2018 update: a report from the American Heart
682 Association. *Circulation.* 2018.
683 58. Drakos SG, Kfoury AG, Hammond EH, Reid BB, Revelo MP, Rasmusson BY, et al.
684 Impact of mechanical unloading on microvasculature and associated central remodeling
685 features of the failing human heart. *Journal of the American College of Cardiology.*
686 2010;56(5):382-91.
687 59. Tsagalou EP, Anastasiou-Nana M, Agapitos E, Gika A, Drakos SG, Terrovitis JV, et al.
688 Depressed coronary flow reserve is associated with decreased myocardial capillary
689 density in patients with heart failure due to idiopathic dilated cardiomyopathy. *Journal of*
690 *the American College of Cardiology.* 2008;52(17):1391-8.
691 60. Parodi O, De Maria R, Oltrona L, Testa R, Sambuceti G, Roghi A, et al. Myocardial
692 blood flow distribution in patients with ischemic heart disease or dilated cardiomyopathy
693 undergoing heart transplantation. *Circulation.* 1993;88(2):509-22.
694 61. Abraham D, Hofbauer R, Schäfer R, Blumer R, Paulus P, Miksovsky A, et al. Selective
695 downregulation of VEGF-A165, VEGF-R1, and decreased capillary density in patients
696 with dilative but not ischemic cardiomyopathy. *Circulation research.* 2000;87(8):644-7.
697 62. Mosseri M, Schaper J, Admon D, Hasin Y, Gotsman M, Sapoznikov D, et al. Coronary
698 capillaries in patients with congestive cardiomyopathy or angina pectoris with patent
699 main coronary arteries. Ultrastructural morphometry of endomyocardial biopsy samples.
700 *Circulation.* 1991;84(1):203-10.
701 63. Miao Y, Tian L, Martin M, Paige SL, Galdos FX, Li J, et al. Intrinsic Endocardial
702 Defects Contribute to Hypoplastic Left Heart Syndrome. *Cell Stem Cell.* 2020;27(4):574-
703 89. e8.

64. Zhao L, Ben-Yair R, Burns CE, and Burns CG. Endocardial Notch Signaling Promotes Cardiomyocyte Proliferation in the Regenerating Zebrafish Heart through Wnt Pathway Antagonism. *Cell Rep.* 2019;26(3):546-54 e5.
65. Shen H, Gan P, Wang K, Darehzereshki A, Wang K, Kumar SR, et al. Mononuclear diploid cardiomyocytes support neonatal mouse heart regeneration in response to paracrine IGF2 signaling. *Elife.* 2020;9:e53071.
66. Lamprecht MR, Sabatini DM, and Carpenter AE. CellProfiler: free, versatile software for automated biological image analysis. *Biotechniques.* 2007;42(1):71-5.
67. Berg S, Kutra D, Kroeger T, Straehle CN, Kausler BX, Haubold C, et al. Ilastik: interactive machine learning for (bio) image analysis. *Nature Methods.* 2019:1-7.
68. Wickham H, Francois R, Henry L, and Müller K. dplyr: A Grammar of Data Manipulation: https://CRAN. *R-project org/package= dplyr.* 2015.
69. Sievert C, Parmer C, Hocking T, Chamberlain S, Ram K, Corvellec M, et al. Plotly: create interactive web graphics via 'plotly. js'. R package. version 4.7. 1; 2017. *URL https://CRAN R-project org/package= plotly.* 2018.
70. Kobayashi Y, Tata A, Konkimalla A, Katsura H, Lee RF, Ou J, et al. Persistence of a regeneration-associated, transitional alveolar epithelial cell state in pulmonary fibrosis. *Nat Cell Biol.* 2020;22(8):934-46.
71. Macosko EZ, Basu A, Satija R, Nemesh J, Shekhar K, Goldman M, et al. Highly Parallel Genome-wide Expression Profiling of Individual Cells Using Nanoliter Droplets. *Cell.* 2015;161(5):1202-14.
72. Butler A, Hoffman P, Smibert P, Papalexi E, and Satija R. Integrating single-cell transcriptomic data across different conditions, technologies, and species. *Nat Biotechnol.* 2018;36(5):411-20.
73. Hewitt FC, Li C, Gray SJ, Cockrell S, Washburn M, and Samulski RJ. Reducing the risk of adeno-associated virus (AAV) vector mobilization with AAV type 5 vectors. *J Virol.* 2009;83(8):3919-29.
74. Lee HK, Widmayer SJ, Huang M-N, Aylor DL, and Marchuk DA. Novel Neuroprotective Loci Modulating Ischemic Stroke Volume in Wild-Derived Inbred Mouse Strains. *Genetics.* 2019;213(3):1079-92.
75. Karra R, Knecht AK, Kikuchi K, and Poss KD. Myocardial NF-kappaB activation is essential for zebrafish heart regeneration. *Proc Natl Acad Sci U S A.* 2015;112(43):13255-60.
76. Purcell S, Neale B, Todd-Brown K, Thomas L, Ferreira MA, Bender D, et al. PLINK: a tool set for whole-genome association and population-based linkage analyses. *Am J Hum Genet.* 2007;81(3):559-75.
77. Burgess S, Dudbridge F, and Thompson SG. Combining information on multiple instrumental variables in Mendelian randomization: comparison of allele score and summarized data methods. *Stat Med.* 2016;35(11):1880-906.
78. Yavorska OO, and Burgess S. MendelianRandomization: an R package for performing Mendelian randomization analyses using summarized data. *Int J Epidemiol.* 2017;46(6):1734-9.
79. Bycroft C, Freeman C, Petkova D, Band G, Elliott LT, Sharp K, et al. The UK Biobank resource with deep phenotyping and genomic data. *Nature.* 2018;562(7726):203-9.

80. Bowden J, Davey Smith G, and Burgess S. Mendelian randomization with invalid instruments: effect estimation and bias detection through Egger regression. *Int J Epidemiol.* 2015;44(2):512-25.
81. Burgess S, Zuber V, Valdes-Marquez E, Sun BB, and Hopewell JC. Mendelian randomization with fine-mapped genetic data: Choosing from large numbers of correlated instrumental variables. *Genet Epidemiol.* 2017;41(8):714-25.
82. Wickham H. ggplot2. *Wiley Interdisciplinary Reviews: Computational Statistics.* 2011;3(2):180-5.
83. Kassambara A. 2017.

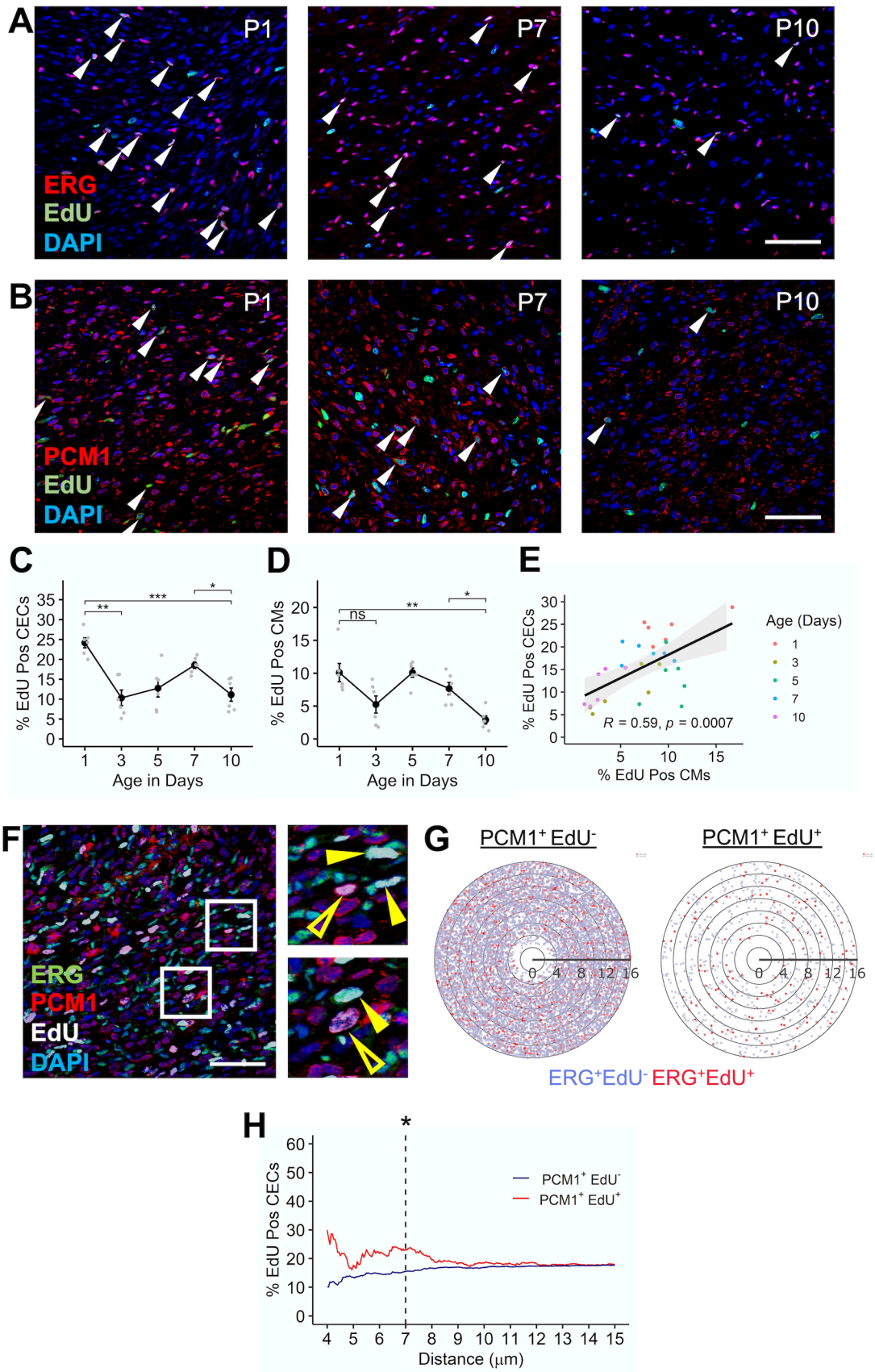
A
P1
P7
P10
ERG
EdU
DAPI
B
P1
P7
P10
PCM1
EdU
DAPI
C
% EdU Pos CECs
Age in Days
D
% EdU Pos CMs
ns
Age in Days
E
% EdU Pos CECs
% EdU Pos CMs
R = 0.59, p = 0.0007
Age (Days)
1
3
5
7
10
F
ERG
PCM1
EdU
DAPI
G
PCM1+ EdU-
PCM1+ EdU+
ERG+EdU- ERG+EdU+
H
% EdU Pos CECs
Distance (μm)
PCM1+ EdU-
PCM1+ EdU+

759

760 **Figure 1. Myovascular coupling during early neonatal growth**. **(A)** Representative images
761 from postnatal day 1 (P1), 7 (P7), and 10 (P10) neonatal mouse hearts immunostained for Erg to
762 mark CECs and EdU to identify proliferating CECs (arrows). **(B)** Representative images
763 immunostained for PCM1 and EdU. Arrows point to EdU^+PCM1^+ proliferating CMs. **(C, D)**
764 Quantitation of CEC and CM proliferation (n = 6 mice per time point). Each gray point is an
765 individual heart. *$p < 0.05$, **$p < 0.01$, ***$p < 0.001$, ns = not significant, two-sided t-test corrected
766 for multiple comparisons using Holm's method. **(E)** Correlation of CEC and CM proliferation.
767 Black line is the best-fit regression line and gray area indicates the 95% CI. p value indicates
768 significance of Pearson correlation. Each point represents an individual heart and is color coded
769 by age. **(F)** Representative image from a P4 heart immunostained for PCM1, Erg, EdU, and DAPI.
770 Boxed regions correspond to the adjacent magnified panels. Hollowed, yellow arrows are
771 $PCM1^+EdU^+$ CMs and solid yellow arrows are Erg^+EdU^+ CECs. **(G)** Pseudodistance maps for
772 detecting enrichment of EdU^+ CECs around EdU^+ CMs. Distance information for 12,374 CEC-
773 CM pairs from 6 mice was used to map EdU^+ CECs (red dots) and EdU^- CECs (blue dots) relative
774 to an averaged EdU^- and EdU^+ CM (center of the plot). Each line represents 2 μm from the center
775 of an averaged CM nucleus. **(H)** Proportion of CEC's that are EdU^+ as a function of distance (μm)
776 from $PCM1^+EdU^+$ nuclei (red) and $PCM1^+EdU^-$ nuclei (blue). 274 EdU^+ CMs and 3658 EdU^- CMs
777 from 6 mice were considered, $p = 0.04$ at 7 μm, two-sided Z-test. Scale bars are 50 μm.
778
779

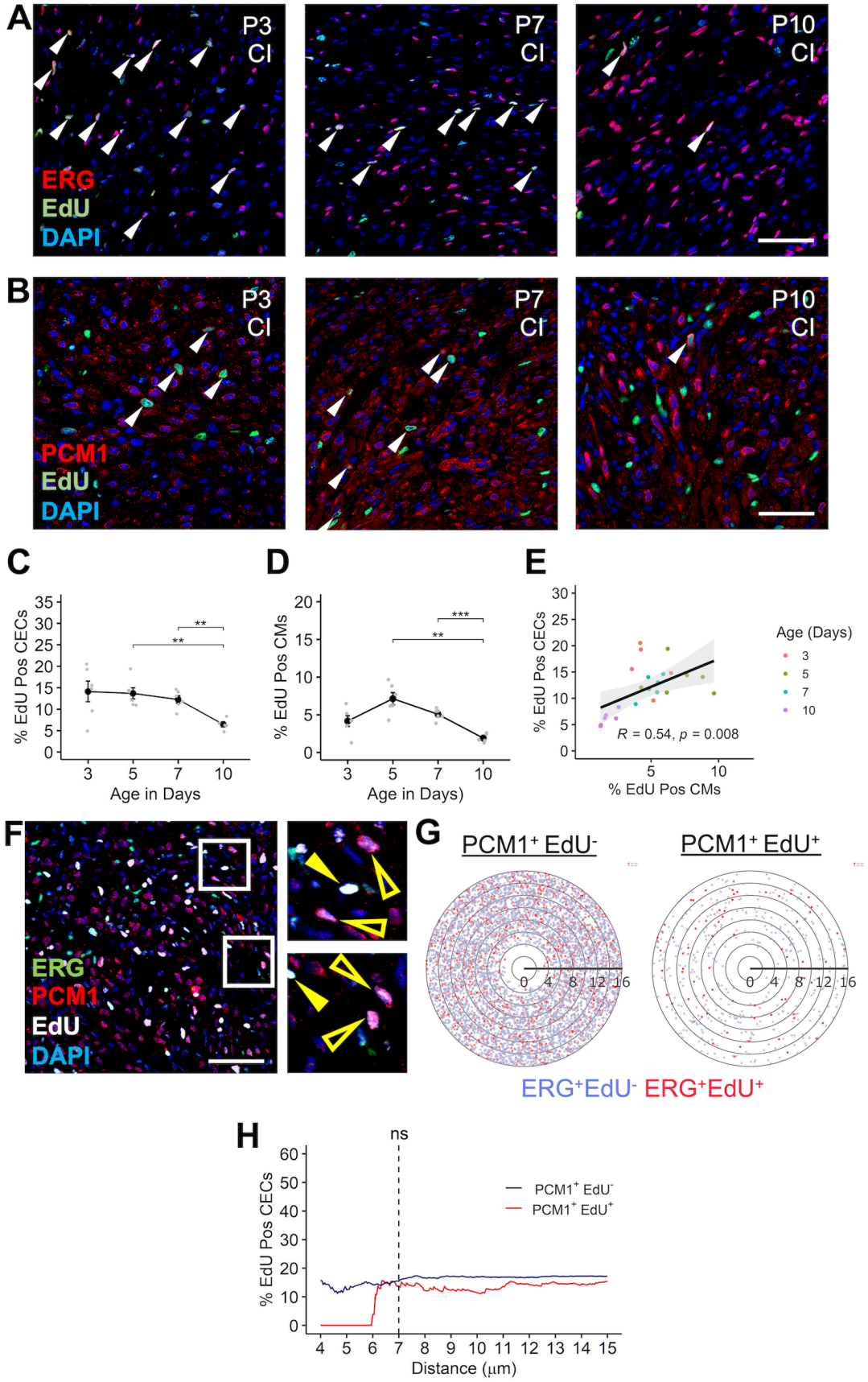
A
P3
CI
P7
CI
P10
CI
ERG
EdU
DAPI
B
P3
CI
P7
CI
P10
CI
PCM1
EdU
DAPI
C
% EdU Pos CECs
Age in Days
D
% EdU Pos CMs
Age in Days)
E
% EdU Pos CECs
% EdU Pos CMs
R = 0.54, p = 0.008
Age (Days)
3
5
7
10
F
ERG
PCM1
EdU
DAPI
G
PCM1+ EdU-
PCM1+ EdU+
ERG+EdU- ERG+EdU+
H
ns
% EdU Pos CECs
Distance (μm)
PCM1+ EdU-
PCM1+ EdU+

780

781 **Figure 2. Myovascular coupling after cryoinjury**. (**A, B)** Representative images from hearts
782 collected at P1, P7, and P10 after cryoinjury (CI) at P1. Arrows point to EdU^+Erg^+ proliferating
783 CECs in (A) and EdU^+PCM1^+ proliferating CMs in (B). **(C, D)** Quantitation of CEC and CM
784 proliferation after CI (n = 5-6 mice per time point). Each gray point is an individual heart. **$p <$
785 0.01, ***$p < 0.001$, two-sided t-test corrected for multiple comparisons using Holm's method. **(E)**
786 Correlation of CEC and CM proliferation. Black line is the best-fit regression line and gray area
787 indicates the 95% CI. p value indicates significance of Pearson correlation. Each point is an
788 individual heart, color coded by age. **(F)** Representative section from the border zone of a
789 cryoinjured P4 heart immunostained for PCM1, Erg, EdU, and DAPI. Boxed regions correspond
790 to the adjacent magnified panels. Hollowed, yellow arrows are $PCM1^+EdU^+$ CMs and solid yellow
791 arrows are Erg^+EdU^+ CECs. **(G)** Pseudodistance maps for detecting enrichment of EdU^+ CECs
792 around EdU^+ CMs. Distance information for 7,093 CEC-CM pairs from 6 mice post CI was used
793 to map EdU^+ CECs (red dots) and EdU^- CECs (blue dots) relative to an averaged EdU^- and EdU^+
794 CM (center of the plot). Each line represents 2 μm from the center of an averaged CM nucleus.
795 **(H)** Proportion of CEC's that are EdU^+ as a function of distance in μm from $PCM1^+EdU^+$ nuclei
796 (red) and $PCM1^+EdU^-$ nuclei (blue). Solid line indicates the point estimate. 186 EdU^+ CMs and
797 2446 EdU^- CMs were considered, p = not significant (ns) at 7 μm, two-sided Z-test. Scale bars are
798 50 μm.
799
800

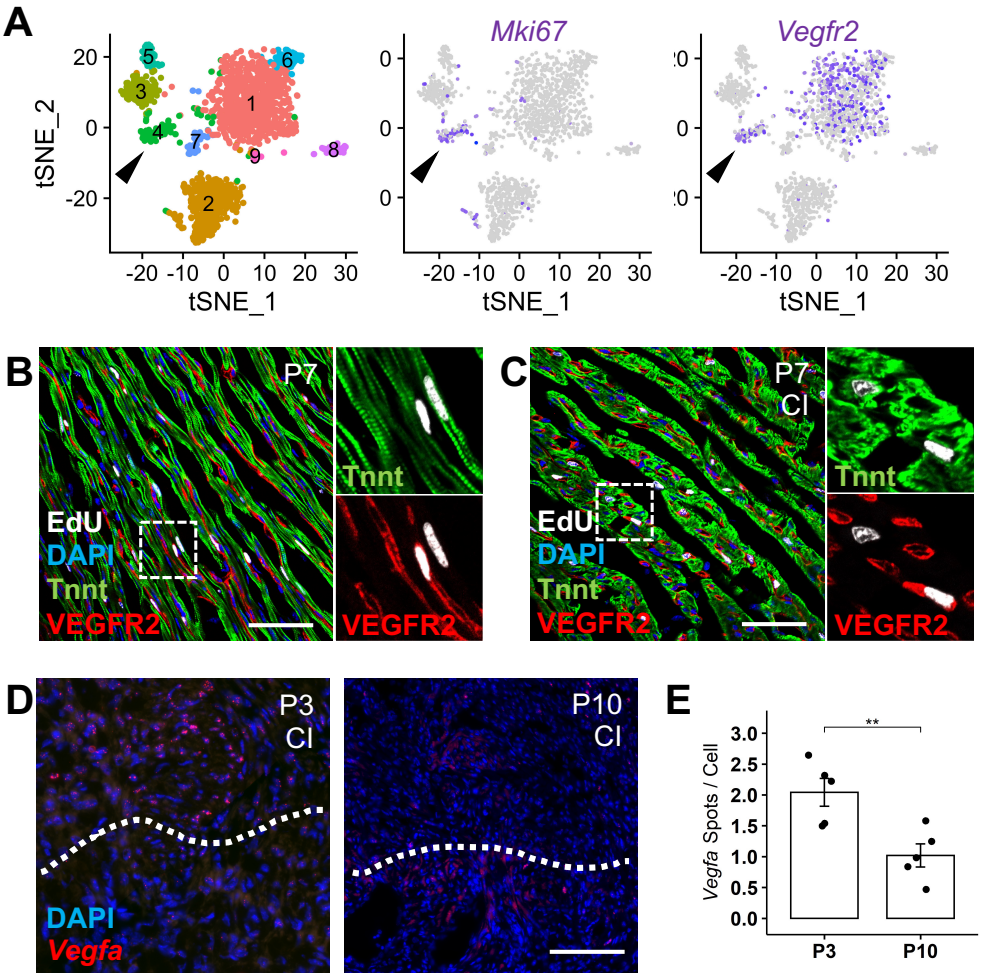
A
tSNE_2
tSNE_1
Mki67
Vegfr2
B
P7
EdU
DAPI
Tnnt
VEGFR2
C
P7
CI
D
P3
CI
P10
CI
DAPI
Vegfa
E
Vegfa Spots / Cell
P3
P10
**

801

802

803 **Figure 3. VEGFA-VEGFR2 signaling is associated with myovascular coupling**. **(A)** tSNE
804 plots of scRNA-seq data from P7 hearts that were underwent CI at P1. In the left most panel,
805 cells are colored by clusters identified by PCA analysis. Arrows point to a cluster of CECs that
806 are enriched for expression of *Mki67* and *Vegfr2* (purple). **(B, C)** Clusters of $EdU^+VEGFR2^+$
807 CECs adjacent to EdU^+Tnnt^+ CMs at P7 during growth (B) and after CI at P1 (C). Insets are
808 magnifications of the regions in the solid white boxes. **(D)** Single molecule in situ hybridization
809 for *Vegfa* in P3 and P10 hearts that underwent CI at P1. Dashed line indicates the approximate
810 injury plane, with the border zone above the line. Red marks *Vegfa* signal. **(E)** Quantitation of in
811 situ hybridization for *Vegfa* expression in the border zone of P3 (n = 5) and P10 (n=5) hearts
812 after CI at P1, **p = 0.008, two-sided t-test. Scale bars are 50 μm.
813
814

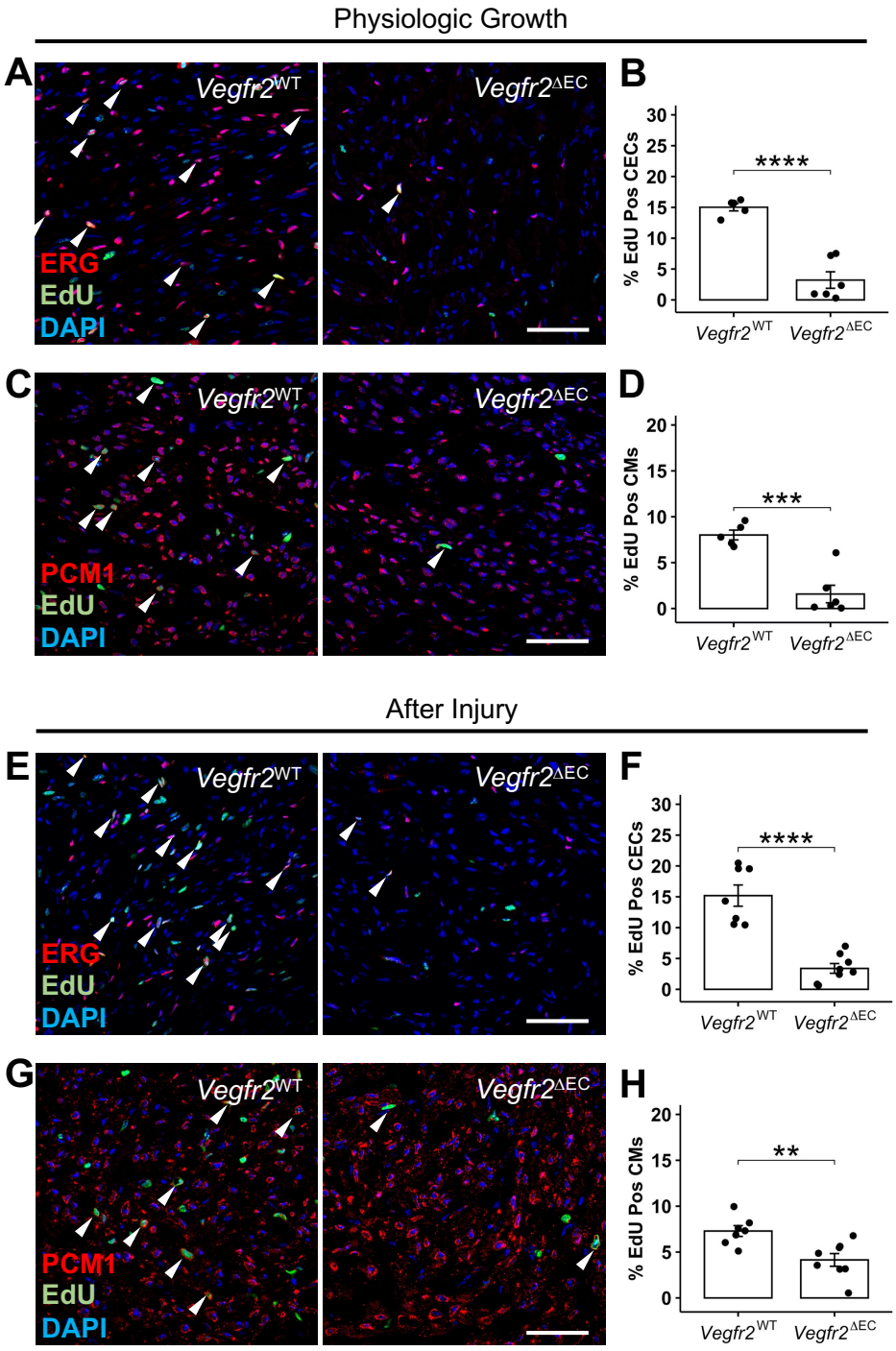
Physiologic Growth
A
Vegfr2WT
Vegfr2ΔEC
ERG
EdU
DAPI
B
% EdU Pos CECs
****
Vegfr2WT
Vegfr2ΔEC
C
PCM1
D
% EdU Pos CMs
***
After Injury
E
F
G
H
**

815

816 **Figure 4: Requirement of *Vegfr2* in CECs for myovascular growth in the neonatal mouse**
817 **heart**. **(A)** Representative images of P4 hearts from *Vegfr2*^{WT} and *Vegfr2*$^{\Delta EC}$ mice, immunostained
818 to detect cycling CECs. Arrows point to EdU^{+} Erg^{+} proliferating CECs. (**B)** Quantitation of CEC
819 proliferation in *Vegfr2*^{WT} (n = 5) and *Vegfr2*$^{\Delta EC}$ mice (n = 6). ****p = 3.7x10^{-5}, two-sided t-test.
820 **(C)** Representative images of P4 hearts from *Vegfr2*^{WT} and *Vegfr2*$^{\Delta EC}$ mice, immunostained to
821 detect cycling CMs. Arrows point to EdU^{+}PCM1^{+} proliferating CMs. **(D)** Quantitation of CM
822 proliferation in *Vegfr2*^{WT} (n = 5) and *Vegfr2*^{DEC} mice (n = 6). ***p = 0.0004, two-sided t-test. **(E)**
823 Images of P4 hearts from *Vegfr2*^{WT} and *Vegfr2*$^{\Delta EC}$ mice after CI at P1. Sections are immunostained
824 to detect cycling CECs. Arrows point to EdU^{+}Erg^{+} proliferating CECs. **(F)** Quantitation of CEC
825 proliferation in *Vegfr2*^{WT} (n = 7) and *Vegfr2*$^{\Delta EC}$ mice (n = 8). ****p = 2.0x10^{-5}, two-sided t-test.
826 **(G)** Representative images of P4 hearts injured at P1 from *Vegfr2*^{WT} and *Vegfr2*$^{\Delta EC}$ mice. Sections
827 are immunostained to detect cycling CMs. Arrows point to EdU^{+}PCM1^{+} proliferating CMs. **(H)**
828 Quantitation of CM proliferation in *Vegfr2*^{WT} (n = 7) and *Vegfr2*$^{\Delta EC}$ mice (n = 8). **p = 0.004,
829 two-sided t-test. Scale bars are 50 μm.
830
831
832

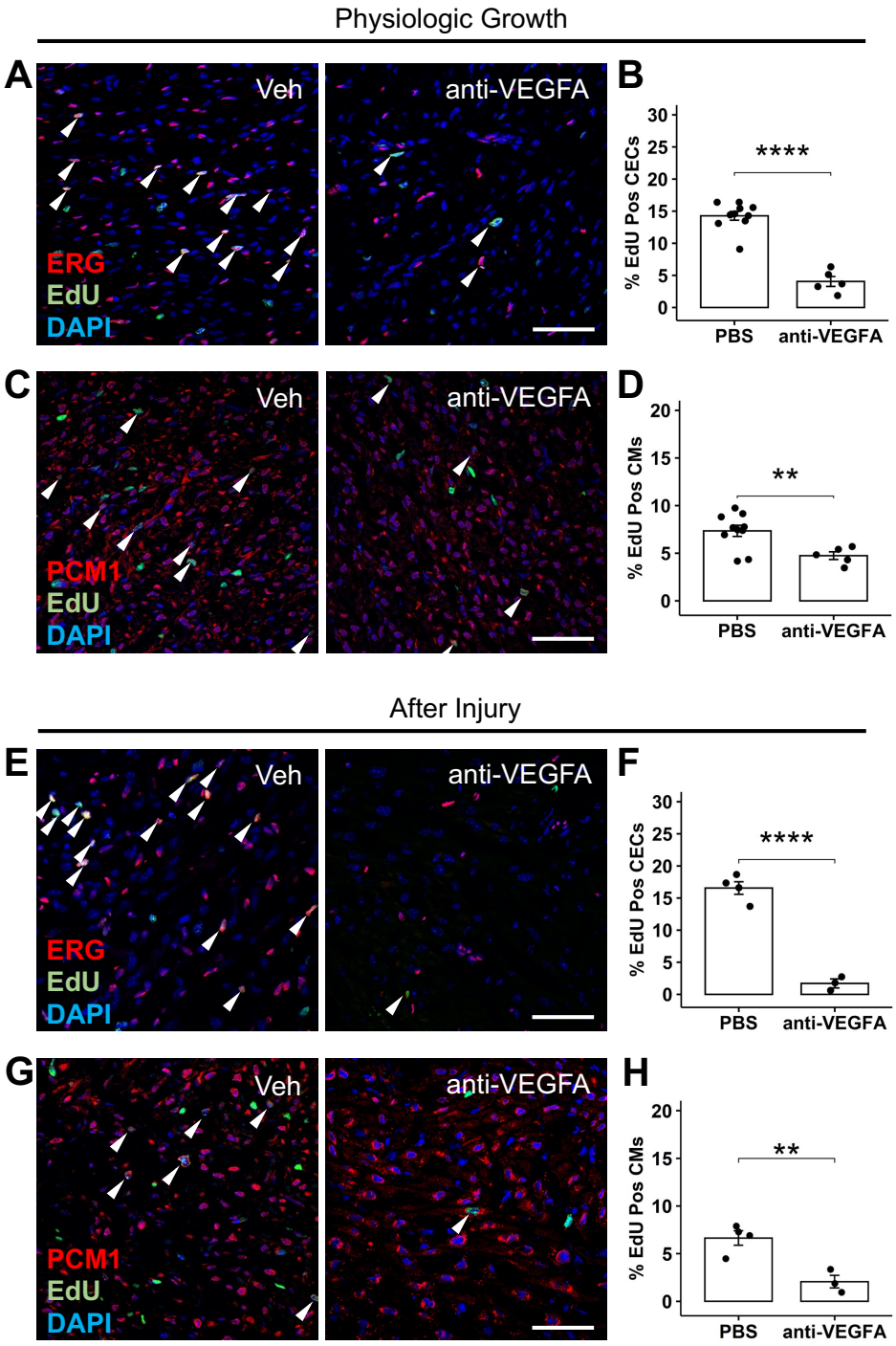
Physiologic Growth
A
Veh
anti-VEGFA
ERG
EdU
DAPI
B
% EdU Pos CECs
****
PBS
anti-VEGFA
C
Veh
anti-VEGFA
PCM1
EdU
DAPI
D
% EdU Pos CMs
**
PBS
anti-VEGFA
After Injury
E
Veh
anti-VEGFA
ERG
EdU
DAPI
F
% EdU Pos CECs
****
PBS
anti-VEGFA
G
Veh
anti-VEGFA
PCM1
EdU
DAPI
H
% EdU Pos CMs
**
PBS
anti-VEGFA

833

834

835 **Figure 5: Requirement of VEGFA for myovascular growth in the neonatal mouse heart**. **(A)**
836 Representative images of P4 hearts from mice injected with vehicle or anti-VEGFA. Sections are
837 immunostained to detect cycling CECs. Arrows point to EdU^+Erg^+ proliferating CECs. **(B)**
838 Quantitation of CEC proliferation at P4 after treatment with vehicle (n = 10) or anti-VEGFA (n =
839 5). ****p = $1.8x10^{-6}$, two-sided t-test. **(C)** Representative images of P4 hearts after treatment with
840 vehicle or anti-VEGFA. Sections are immunostained to detect cycling CMs. Arrows point to
841 EdU^+PCM1^+ proliferating CMs. **(D)** Quantitation at P4 after treatment with vehicle (n = 10) or
842 anti-VEGFA (n = 5). **p = 0.003, two-sided t-test. **(E)** Images of P4 hearts from mice that
843 underwent CI at P1 and that were injected with vehicle or anti-VEGFA. Arrows point to EdU^+Erg^+
844 proliferating CECs. **(F)** Quantitation of CEC proliferation in *Vegfr2*^{WT} (n = 4) and *Vegfr2*$^{\Delta EC}$ mice
845 (n = 3). ****p = $6.9x10^{-5}$, two-sided t-test. **(G)** Immunostaining for PCM1 and EdU in P4 hearts
846 from mice that underwent CI at P1 and that were treated with vehicle or anti-VEGFA. Arrows
847 point to EdU^+PCM1^+ proliferating CMs. **(H)** Quantitation of CM proliferation after treatment with
848 vehicle (n = 4) or anti-VEGFA (n = 3). **p = 0.008, two-sided t-test. Scale bars are 50 μm.
849
850

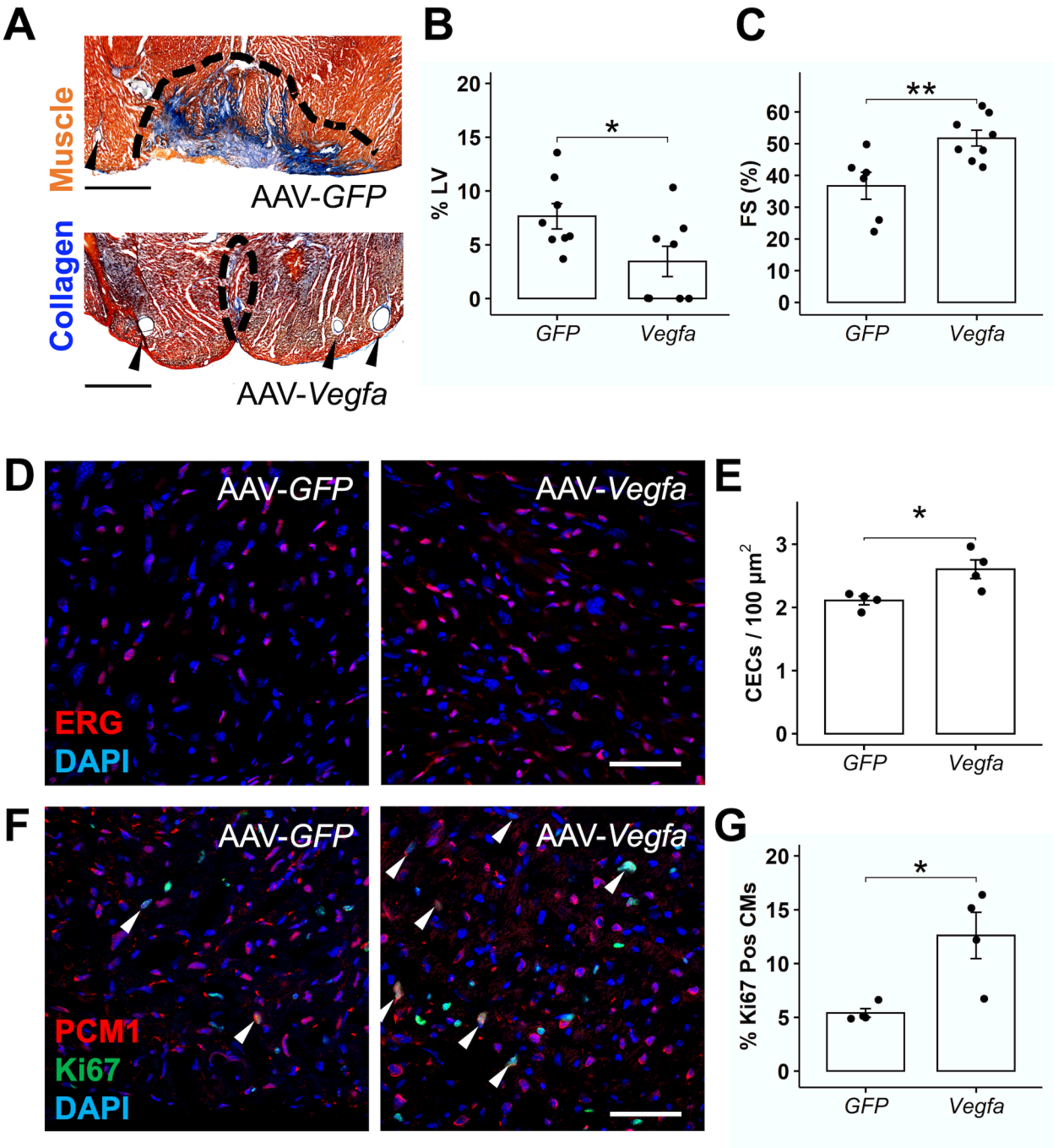
A
Muscle
Collagen
AAV-GFP
AAV-Vegfa
B
% LV
20
15
10
5
0
*
GFP
Vegfa
C
FS (%)
60
50
40
30
20
10
0
**
GFP
Vegfa
D
AAV-GFP
AAV-Vegfa
ERG
DAPI
E
CECs / 100 µm2
3
2
1
0
*
GFP
Vegfa
F
AAV-GFP
AAV-Vegfa
PCM1
Ki67
DAPI
G
% Ki67 Pos CMs
20
15
10
5
0
*
GFP
Vegfa

851

852

853 **Figure 6: Effect of *Vegfa* overexpression on regeneration after CI**. **(A)** AFOG staining of P21
854 hearts to visualize scar (blue). Arrows indicate vessels. Scale bar is 500 μm. **(B)** Quantitation of
855 scar as a percentage of the left ventricle at P21 in animals injected with AAV-*GFP* (n = 8) or
856 AAV-*Vegfa* (n= 8) at the time of CI at P1. *p = 0.038. **(C)** Fractional shortening at P21 in animals
857 injected with AAV-*GFP* (n=6) or AAV-*Vegfa* (n=8) at the time of CI at P1. **p = 0.008, two-
858 sided t-test. **(D)** Images of the border zone from P10 mice that underwent CI at P1. Sections are
859 immunostained to mark proliferating Erg^+ $Ki67^+$ CECs (arrows). **(E)** Quantitation of CEC density
860 at P14 after injection with AAV-GFP (n=4) or AAV-*Vegfa* (n = 4). *p = 0.035, two-sided t-test.
861 **(F)** Images of the border zone from P14 mice that underwent CI at P1. Sections are immunostained
862 to mark proliferating $PCM1^+Ki67^+$ CMs (arrows). **(G)** Quantitation of CM proliferation at P14
863 after injection with AAV-*GFP* (n = 4) or AAV-*Vegfa* (n = 4). *p =0.017, two-sided t-test.
864

865

866

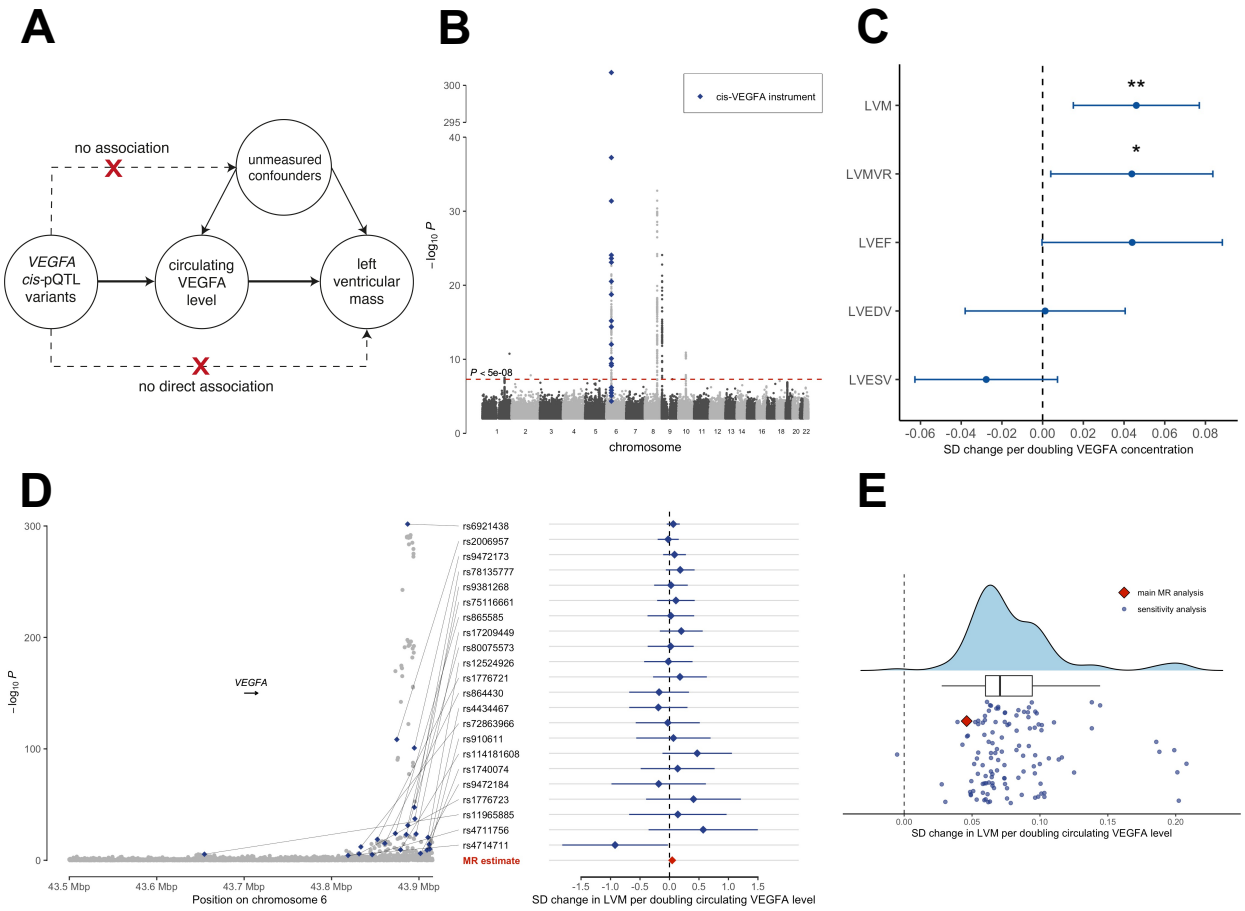
A
no association
unmeasured confounders
VEGFA cis-pQTL variants
circulating VEGFA level
left ventricular mass
no direct association
B
cis-VEGFA instrument
P < 5e-08
chromosome
C
LVM
LVMVR
LVEF
LVEDV
LVESV
SD change per doubling VEGFA concentration
D
VEGFA
Position on chromosome 6
MR estimate
SD change in LVM per doubling circulating VEGFA level
E
main MR analysis
sensitivity analysis
SD change in LVM per doubling circulating VEGFA level

867 **Figure 7: Effect of circulating VEGFA levels on human cardiac structure. (A)** Illustrative
868 diagram of *cis*-Mendelian randomization (cis-MR) design to estimate the causal association
869 between circulating VEGFA level and left ventricular mass (LVM). **(B)** Manhattan plot showing
870 genome-wide genetic association with circulating VEGFA level. **(C)** *cis*-Mendelian randomization
871 estimate with inverse-variance weighted model of circulating VEGFA level on left ventricular end-
872 diastolic volume (LVEDV), left ventricular end systolic volume (LVESV), left ventricular ejection
873 fraction (LVEF), left ventricular mass to volume ratio (LVMR), and LV mass (LVM). Each data
874 point represents effect estimate in standard deviation (SD) change of the trait per doubling the
875 circulating VEGFA concentration. Error bars indicate 95% confidence intervals (CI) of the
876 estimates. *$p < 0.05$, **$p < 0.01$. **(D)** Regional genetic association plot for *cis*-region of the *VEGFA*
877 gene (200 kilobase flanking region from transcript start and end sites) with *cis*-instruments for the
878 main Mendelian randomization analysis highlighted. Estimated causal effects on LVM for each
879 instrument are shown on the right panel with error bars representing 95% confidence interval. **(E)**
880 Distribution of point estimates showing standard deviation (SD) gram change in LVM per
881 doubling circulating VEGFA level as estimated with *cis*-MR with IVW model (red diamond) and
882 sensitivity analyses with permutation of instrument selection methods and *cis*-MR models.
883
884
885

886 **Supplemental Figures**

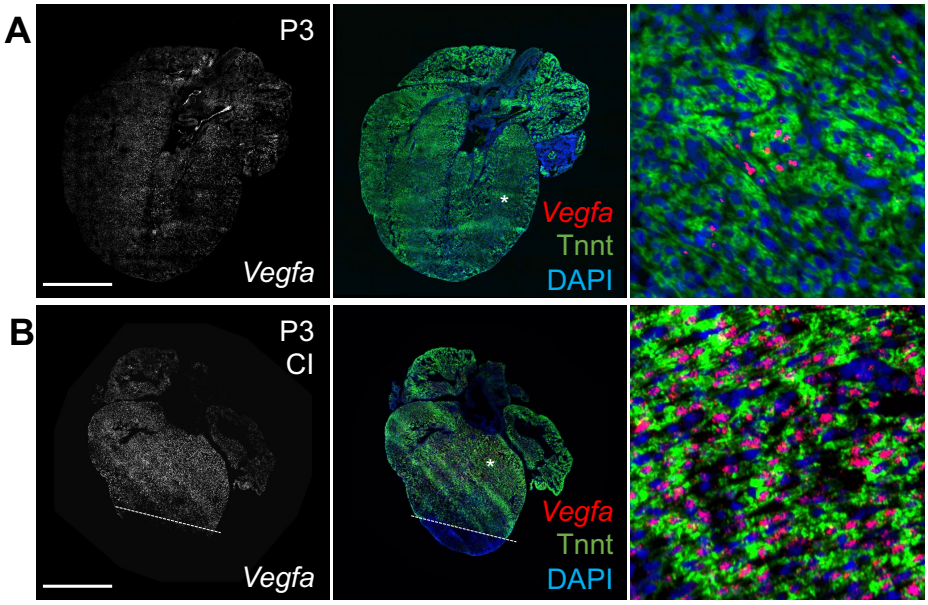

887

888 **Figure S1. *Vegfa* expression in the neonatal mouse heart**. **(A-B)** Tilescan images of an
889 uninjured P3 heart (A) and a P3 heart that underwent CI at P1 (B). Sections are immunostained
890 for Tnnt (green) and hybridized with an in situ probe for *Vegfa* (red). Lines correspond to the
891 approximate injury plane. The asterisks correspond to the magnified images. Scale bar is 500
892 μm.

893

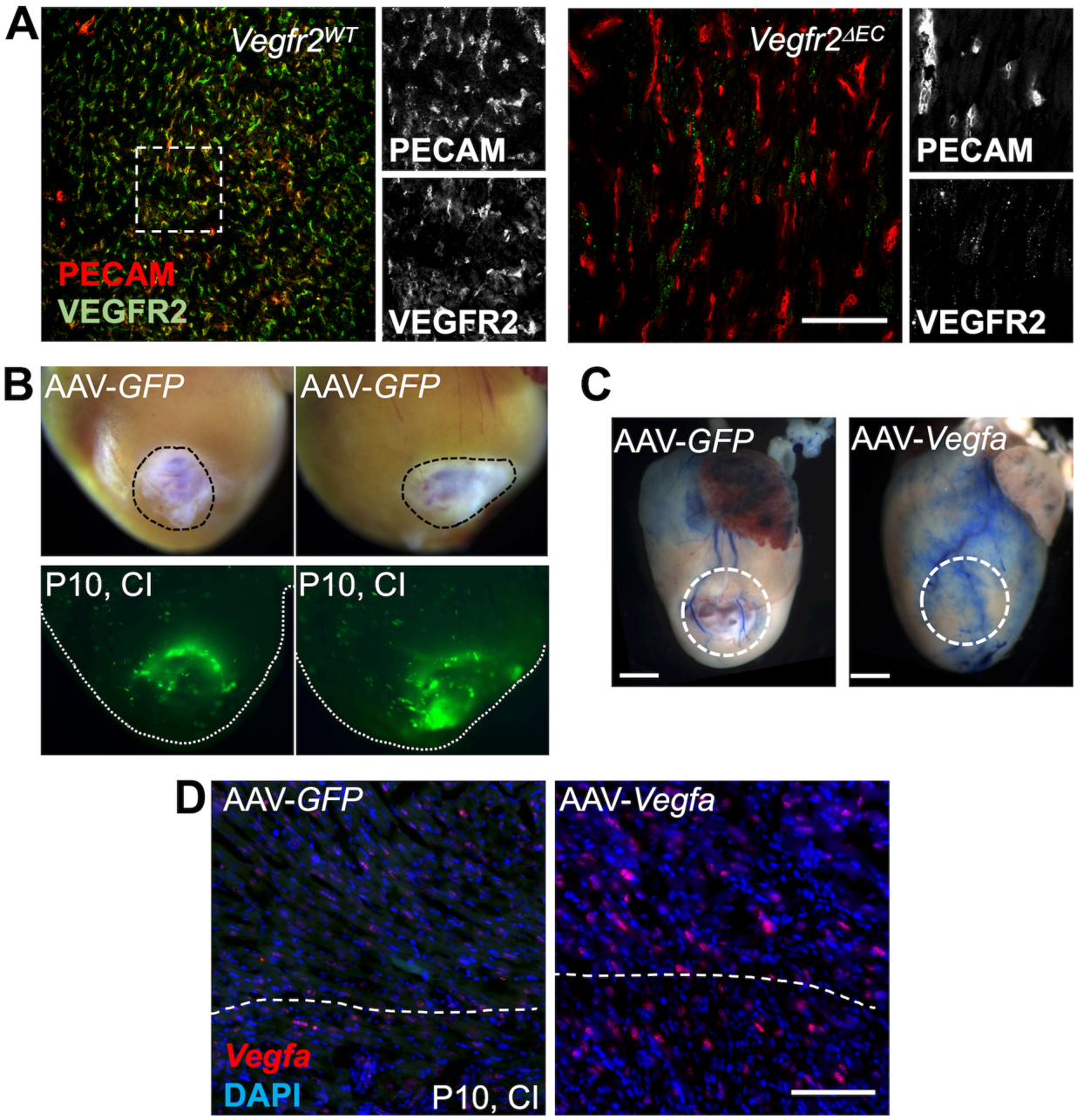

894

895 **Figure S2. Approaches to manipulate VEGFA/VEGFR2 signaling**. **(A)** Images of *Vegfr2*^{WT}
896 and *Vegfr2*$^{\Delta EC}$ mice at P3 after treatment with tamoxifen at P0. Sections are immunostained for
897 PECAM and VEGFR2. The dashed box corresponds to magnified images, shown as individual
898 channels. Scale bar is 100 µm. **(B)** Whole mount images of representative P10 hearts injected
899 with AAV-*GFP* at the time of CI at P1. (Top) Brightfield images of the ventricles with the black
900 dashed circle indicating the area of injury. (Bottom) Corresponding GFP images to show
901 concentration of GFP expression around the area of injury. **(C)** Whole mount images of

902 representative P21 hearts, injected with either AAV-*GFP* or AAV-*Vegfa* at the time of CI at P1.
903 Blue resin opacifies the coronary vasculature. Circled area indicates the approximated area of
904 injury. Scale bar is 1 μm. **(D)** Single molecule in situ hybridization for *Vegfa* in the border zone
905 of P10 hearts that were injected with either AAV-*GFP* or AAV-*Vegfa* after CI at P1. Dashed line
906 indicates the approximate plane of injury, with the region above the line corresponding to the
907 border zone. Red dots indicate *Vegfa* expression. Scale bar is 50 μm.
908

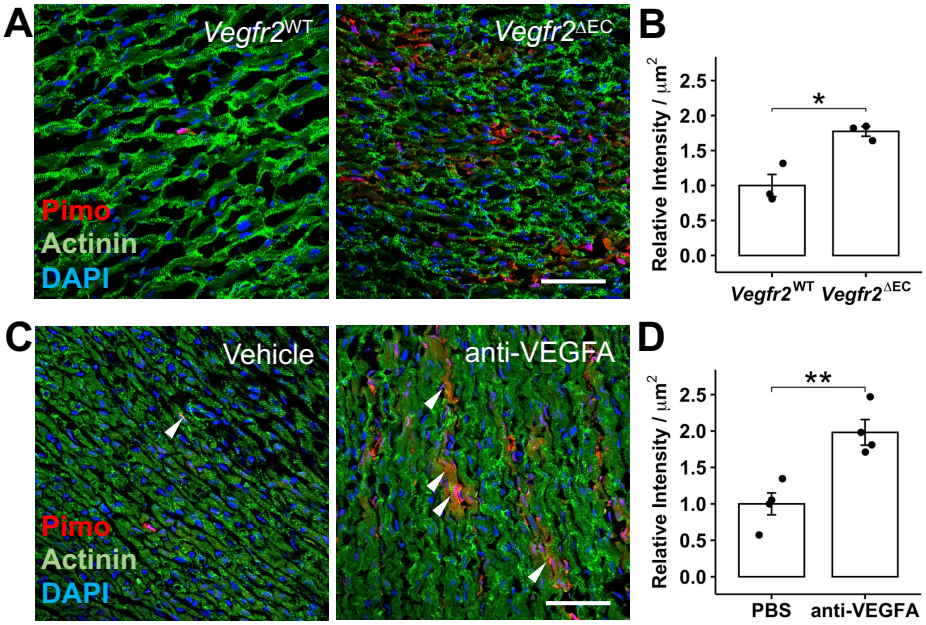

Figure S3: Myocardial hypoxia with loss of *Vegfr2* in CECs or after administration of anti-VEGFA. **(A)** Images of sections from P4 *Vegfr2*^{WT} and *Vegfr2*$^{\Delta EC}$ hearts immunostained for actinin (green) and pimonidazole (red) incorporation. **(B)** Quantitation of pimonidazole intensity per µm of tissue stained with actinin in *Vegfr2*^{WT} (n = 3) and *Vegfr2*$^{\Delta EC}$ (n = 3) hearts. *p = 0.011, two-sided t-test. **(C)** Images of sections from P4 mice treated with vehicle or anti-VEGFA. Sections are immunostained for actinin (green) and pimonidazole (red) incorporation. **(D)** Quantitation of pimonidazole intensity per µm of tissue stained with actinin in mice treated with vehicle (n = 4) or anti-VEGFA (n=4). **p = 0.005, two-sided t-test. Scale bars are 50 µm.

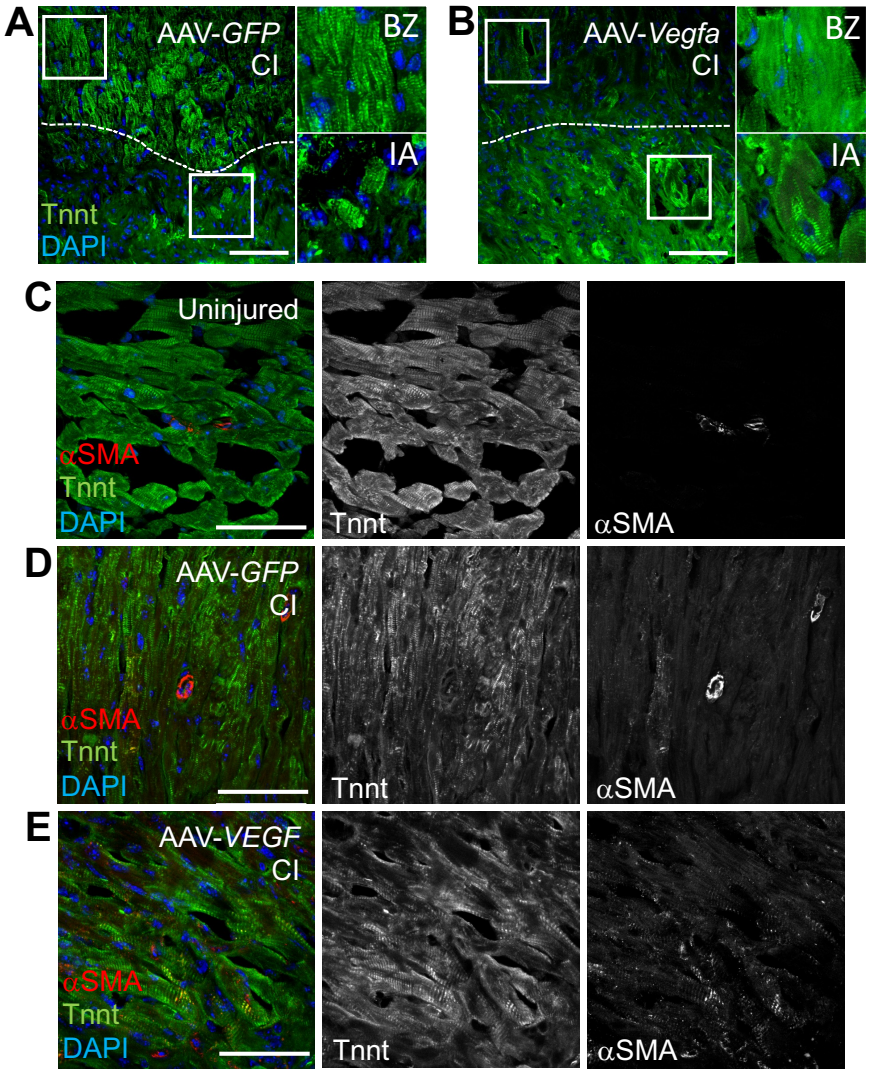

Figure S4: Effect of *Vegfa* overexpression on sarcomere morphology and αSMA expression in CMs after CI. **(A-B)** Images from the site of injury of P21 mice that were treated with AAV-*GFP* or AAV-*Vegfa* at the time of CI at P1. Dashed line indicates the approximate plane of injury. The region above the line is the border zone (BZ) and the region below the line is the injured area (IA). Boxed regions correspond to the adjacent magnified panels. Sections are immunostained for the sarcomeric protein Tnnt (green). **(C-E)** Images of the border zone from P21 mice that underwent injection of AAV-*GFP* **(D)** or AAV-*Vegfa* **(E)** at time of CI at P1 or physiological control **(C)**. Sections are immunostained to mark CMs (Tnnt, green) and alpha-smooth muscle actin (αSMA, red). Scale bars are 50 μm.